

Can the magmatic conditions of the Martian nakhlites be discerned via investigation of clinopyroxene and olivine crystallographic slip-systems?

Sammy Griffin¹, Luke Daly¹, Sandra Piazzolo², Lucy V Forman³, Benjamin E Cohen⁴, Martin Lee¹, Patrick W Trimby⁵, Raphaël Baumgartner⁶, Gretchen K Benedix³, and Ben Hoefnagels⁷

¹University of Glasgow

²School of Earth and Environment, The University of Leeds

³Curtin University

⁴University of Edinburgh

⁵Oxford Instruments

⁶Unknown

⁷CityGIS

November 22, 2022

Abstract

Deformation is a near ubiquitous process that is observed within nearly all naturally forming rocks, terrestrial and extra-terrestrial. Large area electron backscatter diffraction (EBSD) is a technique that enables slip-systems (a form of plastic deformation) to be inferred at a comparable scale to representative texture analysis ([?]100 crystals). Extensive laboratory and studies on naturally occurring samples have identified preferential extrinsic parameters for specific slip-system signatures within olivine and clinopyroxene for mantle conditions. Slip-systems in both olivine and augite (high Ca-clinopyroxene) for 21 large area EBSD datasets sourced from 16 different Martian nakhlite meteorites were analysed and assessed against these parameters. When investigating the high and low deformation regions within the samples 10 of the 21 sections exhibited a shift in the slip-system patterns between the low and high deformation regions. The secondary signatures identified within the low deformation regions are inferred to relate to emplacement deformation. Thus, these samples exhibit both shock and emplacement signatures. The observed variations in deformation patterns for the two main regimes of deformation indicate heterogeneous sampling of the nakhlite ejecta crater. Our findings indicate that shock deformation is prevalent throughout the nakhlites, and that great care needs to be taken when interpreting slip-deformation of crystals within apparent lower deformation regions.

1 **Can the magmatic conditions of the Martian nakhlites be discerned via investigation**
2 **of clinopyroxene and olivine crystallographic slip-systems?**

3 **S. Griffin¹, L. Daly^{1,2,3,4}, S. Piazzolo⁵, L. V. Forman², B. E. Cohen⁶, M. R. Lee¹, P. W.**
4 **Trimby⁷, R. J. Baumgartner^{8,9}, G. K. Benedix^{2,10,11}, and B. Hoefnagels.**

5 ¹School of Geographical and Earth Sciences, University of Glasgow, UK.

6 ²Space Science and Technology Centre, School of Earth and Planetary Sciences, Curtin
7 University, Australia.

8 ³Australian Centre for Microscopy and Microanalysis, The University of Sydney, Australia.

9 ⁴Department of Materials, University of Oxford, UK.

10 ⁵School of Earth and Environment, University of Leeds, UK.

11 ⁶Department of Materials, University of Oxford, UK. ⁵School of Geosciences, University of
12 Edinburgh, UK.

13 ⁷Oxford Instruments Nano analysis, High Wycombe, UK.

14 ⁸School of Biological, Earth and Environmental Sciences, The University of New South Wales,
15 Kensington, NSW, Australia.

16 ⁹CSIRO Mineral Resources, Australian Resources Research Centre, Kensington, WA, Australia.

17 ¹⁰Department of Earth and Planetary Sciences, Western Australia Museum, Australia.

18 ¹¹Planetary Institute, USA.

19 Corresponding author: Sammy Griffin (Sammy.Griffin@glasgow.ac.uk)

20 **Key Points:**

- 21 • Large area EBSD reveals shock-derived deformation to mask non-shock deformation
22 even in low deformation regions in the nakhlites.
- 23 • Slip-system patterns indicate nine distinct derived deformation signatures for the
24 nakhlites, interpreted as shock-induced deformation.
- 25 • Non-shock derived slip-system patterns are identified within low deformation regions
26 interpreted as emplacement deformation.
27

28 **Abstract**

29 Deformation is a near ubiquitous process that is observed within nearly all naturally forming
30 rocks, terrestrial and extra-terrestrial. Large area electron backscatter diffraction (EBSD) is a
31 technique that enables slip-systems (a form of plastic deformation) to be inferred at a comparable
32 scale to representative texture analysis (≥ 100 crystals). Extensive laboratory and studies on
33 naturally occurring samples have identified preferential extrinsic parameters for specific slip-
34 system signatures within olivine and clinopyroxene for mantle conditions. Slip-systems in both
35 olivine and augite (high Ca-clinopyroxene) for 21 large area EBSD datasets sourced from 16
36 different Martian nakhlite meteorites were analysed and assessed against these parameters. When
37 investigating the high and low deformation regions within the samples 10 of the 21 sections
38 exhibited a shift in the slip-system patterns between the low and high deformation regions. The
39 secondary signatures identified within the low deformation regions are inferred to relate to
40 emplacement deformation. Thus, these samples exhibit both shock and emplacement signatures.
41 The observed variations in deformation patterns for the two main regimes of deformation
42 indicate heterogeneous sampling of the nakhlite ejecta crater. Our findings indicate that shock
43 deformation is prevalent throughout the nakhlites, and that great care needs to be taken when
44 interpreting slip-deformation of crystals within apparent lower deformation regions.

45 **Plain Language Summary**

46 Clinopyroxene and olivine are important minerals for studying igneous processes on Mars and
47 Earth (from the surface to the upper mantle). Here, clinopyroxene and olivine slip-system
48 patterns - deformational movement within a crystal - were investigated using the specialist
49 microscopic technique of electron backscatter diffraction (EBSD), which enables the
50 identification of crystal structures within a group of Martian meteorites known as the nakhlites.
51 The nakhlites are mafic rocks representing the largest collection of rocks from a singular – but as
52 yet unknown – location on Mars. Combined slip-system patterns for both olivine and
53 clinopyroxene reveal nine different shock deformation signatures for the nakhlites indicating that
54 they were sourced from multiple locations within the ejection crater. Non-shock related
55 deformation can also be observed but tends to be masked by the dominance of shock
56 deformation features even in low deformation regions.

57 **1 Introduction**

58 Deformation within rocks is driven by a wide variety of geological processes *e.g.*,
59 compaction (mountain building, subduction, burial), extension (rifting), shear (flow, faulting),
60 and dramatic changes in both temperature (contact metamorphism, melting/recrystallisation,
61 hypervelocity impacts, and hydrothermal activity) and pressure (hypervelocity impacts, rapid
62 burial). Extrinsic parameters present over a rocks geological history will impact the way each
63 crystal within the sample will grow and deform. Mineral deformation within rocks can occur via
64 several mechanisms including elastic, brittle, and ductile deformation. Where ductile
65 deformation including dislocation creep, diffusion creep, and dissolution-precipitation creep.
66 Microstructures and defects (*e.g.*, dislocations) present within a mineral's crystal lattice record
67 important information pertaining to its crystal plastic deformation (Ashby, 1970, 1983; Fleck et
68 al., 1994; Poirier, 1975, 1985, 1995; Poirier & Nicolas, 1975; Sciences, 1978; Stocker & Ashby,
69 1973). Plastic deformation, a stress and or strain derived permanent change lacking brittle failure
70 or volume change within a material, is typically accommodated at the nano-meter scale by

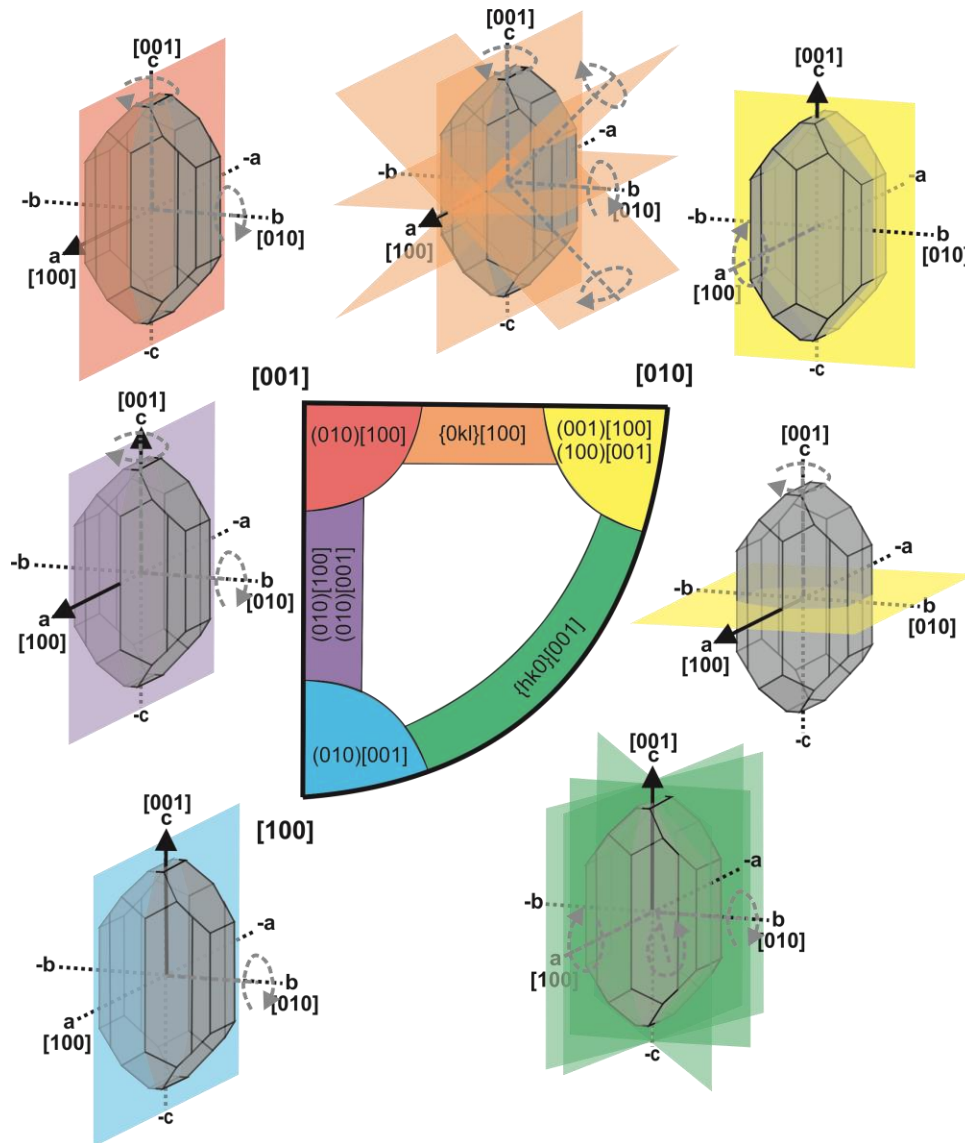
71 crystallographic slip or rotation. Crystallographic slip-systems are directional movement of
72 either slip or rotation which occurs around specific crystallographic axes within either the crystal
73 lattice, sub-boundaries, or inequant crystals (Law, 1990). Within geological specimens, plastic
74 deformation has been shown to develop through either crystallisation processes *e.g.*, mantle/flow
75 rheology, growth twins, (Cordier, 2002; Fei et al., 2012; Frets et al., 2012; Henry et al., 2017;
76 Yao et al., 2019; Zhang et al., 2006) and/or subsequent modification processes *e.g.*, metamorphic
77 shear, mineralogical dehydration/degassing, compaction, or shock (Friedrich et al., 2017; Godard
78 & van Roermund, 1995; van Roermund & Boland, 1981; Ruzicka & Hugo, 2018; Tasaka et al.,
79 2008; Yao et al., 2019). The accumulation of these deformation microstructures, when combined
80 across a representative area of a rock, produce a macroscale pattern of plastic deformation. This
81 macroscale pattern is reported within geological samples as crystallographic preferred
82 orientations (CPO) also known as lattice preferred orientation (LPO), which refers to the nature
83 and extent of orientation of the crystal lattice axis with respect to a specific phase within the
84 sample (Bernard et al., 2019; Hunter, 1996; Mainprice et al., 2015).

85 Previous studies of crystallographic dislocation systems, have shown an activation
86 dependence of slip around specific crystallographic axes, when a crystal is exposed to a
87 differential stress under varying extrinsic conditions *e.g.*, stress, strain, temperature, pressure,
88 and water content (*e.g.*, Raterron and Jaoul, 1991; Katayama et al., 2004; Karato et al., 2008;
89 Raterron et al., 2011; Bernard et al., 2019; Liu et al., 2019). Subsequently, by identifying and
90 characterising the dominant crystallographic dislocation systems activated within particular
91 minerals through extensive laboratory experiments and studies of naturally occurring samples,
92 the ability to broadly ascertain the environment (pressure, temperature, stress, strain, and water
93 content) parameters a rock experienced during deformation has started to develop which can be
94 utilised to provide insight into a given sample's geological history (Barber et al., 2010).
95 However, despite the wealth of information that is stored within crystallographic dislocations
96 and the ever-increasing body of literature, there is a lot about these systems that yet to be fully
97 utilised and understood.

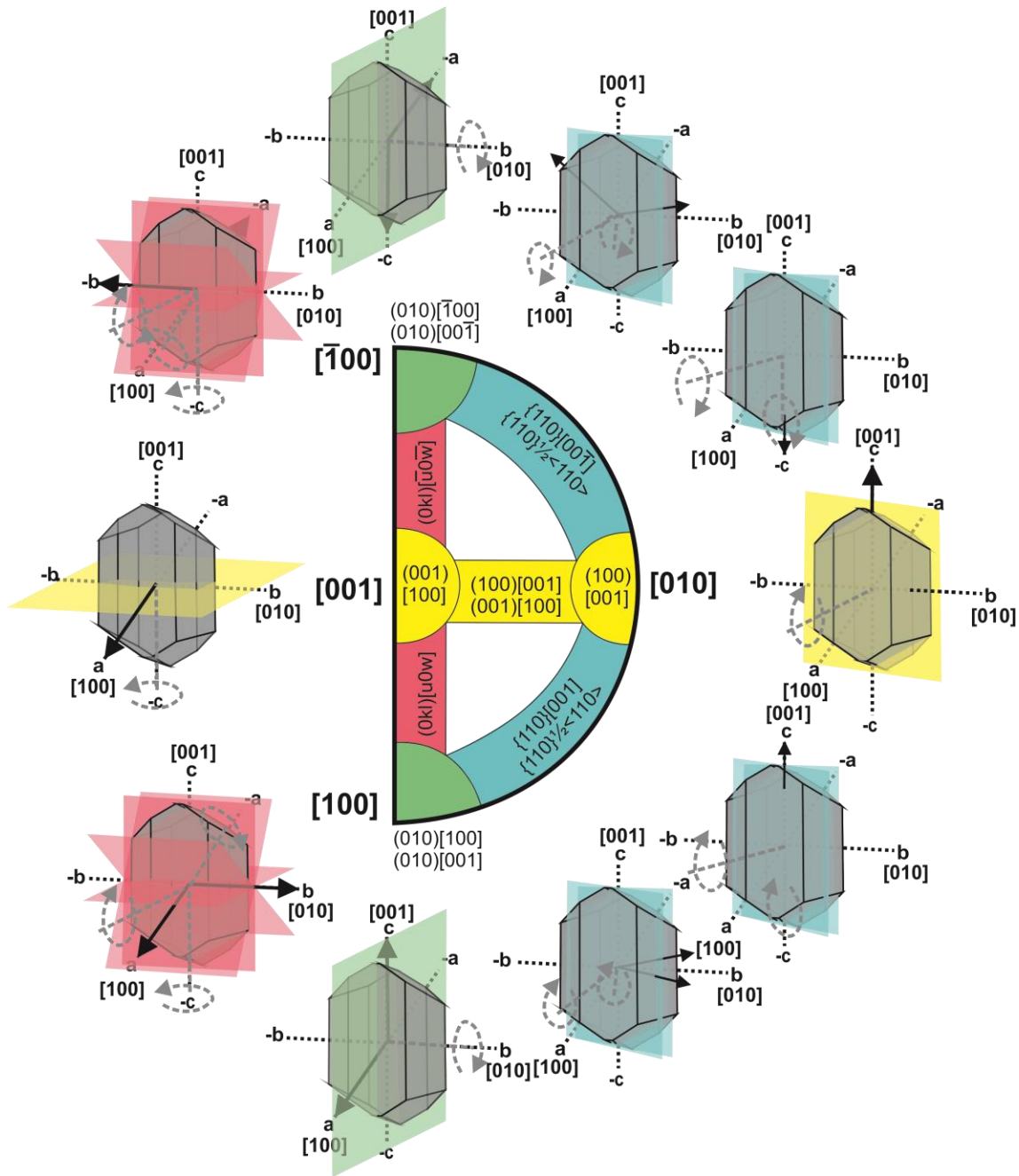
98 Intrinsic controls (*e.g.*, chemistry) alongside extrinsic controls (*e.g.*, temperature,
99 pressure, stress magnitude and strain rate) have long been recognised as important factors for the
100 activation of crystallographic slip-systems in minerals (Ashby, 1983; Barber et al., 2010;
101 Bernard et al., 2019; Groves & Kelly, 1963; Jaoul & Raterron, 1994; Müller et al., 2008; Poirier,
102 1982; Woodward, 2005). However, recent studies of olivine have shown that there are additional
103 factors that can also influence the activation of a given slip-system (Barber et al., 2010; Bernard
104 et al., 2019). These factors include the mechanism of deformation, water content, deformation
105 geometry, presence of melt, and previous deformation history (Boneh & Skemer, 2014; Hansen
106 et al., 2014; H. Jung et al., 2006; Haemyeong Jung et al., 2009; Katayama & Karato, 2006;
107 Précigout & Hirth, 2014; Qi et al., 2018; Sundberg & Cooper, 2008). These other identified
108 factors have the capacity to shift the previously identified activation boundaries of specific slip-
109 systems, related to the minerals chemistry, and the local temperature, pressure, and time frame
110 over which deformation occurs. This is why slip-systems observed in some naturally occurring
111 samples show slip-system signatures at lower extrinsic values compared to those determined
112 from laboratory experiments (Bernard et al., 2019).

113 Here the activation of crystallographic slip-systems within olivine and augite (high Ca-
114 clinopyroxene; Fig. 1, 2), representatives of the orthorhombic and monoclinic crystal systems,

115 respectively, are assessed. Olivine has been extensively studied, both experimentally and in
116 naturally occurring samples of mantle rocks, due to its high-abundance in the Earth's upper
117 mantle which enables insight into the mantle's structure and seismic anisotropy (Bernard et al.,
118 2019; Kaboli et al., 2017; Li et al., 2020; Mainprice et al., 2005; Mei & Kohlstedt, 2000; Poirier,
119 1975; Soustelle & Manthilake, 2017). Thus, the activation criteria for olivine's crystallographic
120 slip-systems over a variety of extrinsic pressure, temperature, stress, strain, and water contents
121 are fairly well constrained (Bernard et al., 2019; Karato et al., 2008; Katayama & Karato, 2006).
122 Augite, on the other hand, is only starting to be studied in the same level of detail (Tedonkenfack
123 et al., 2021; Van Der Werf et al., 2017). Previous work exploring slip-systems in clinopyroxene
124 has predominantly focused on diopside (monoclinic with a similar crystal lattice structure to
125 augite), but mostly in laboratory settings; many of the crystallographic slip-systems observed
126 experimentally have not yet been observed within naturally occurring terrestrial rocks (Bascou et
127 al., 2002; Bystricky & Mackwell, 2001; Ingrin et al., 1991; Jaoul & Raterron, 1994; Mauler et
128 al., 2000; Skrotzki, 1994). However, studies focused on observing clinopyroxene
129 crystallographic slip-systems and CPO in a natural occurring samples has started to increase
130 (Keppler, 2018; Skrotzki, 1994; Tedonkenfack et al., 2021; Van Der Werf et al., 2017). From
131 current limited knowledge of clinopyroxene crystallographic dislocation systems [often based off
132 numerical simulations *e.g.*, Ulrich & Mainprice (2005)], there is a strong dependence on the
133 mineral's orientation relative to the principal stress axes. Observations of clinopyroxene indicate
134 that a dominant slip-system signature pairing dominant (100)[001] with minor (001)[100] (Fig.
135 2) will form under most Earth relevant extrinsic conditions (Kollé & Blacic, 1982; P. Raterron et
136 al., 1994).



137
 138 **Figure 1.** Olivine (forsterite; *mmm*; unit cell lengths $a = 0.466$, $b = 1$, $c = 0.587$) crystallographic
 139 slip-system signature key (notated as the slip plane and slip direction) expressed as the
 140 orthorhombic crystallographic fundamental sector [lowest form of crystal symmetry; modified
 141 from Ruzicka and Hugo (2018)]. The corners of the key refer to olivine's specific
 142 crystallographic axis ($\langle a \rangle = [100]$, $\langle b \rangle = [010]$, and $\langle c \rangle = [001]$). The surrounding diagrams
 143 visualise the different slip planes where the straight black arrows indicate the direction of slip for
 144 both twist and tilt boundaries. For a tilt boundary [movement perpendicular (axis parallel) to the
 145 plane] the black arrows also indicate the tilt axis whereas the plane rotation axis for a twist (*i.e.*,
 146 rotating) boundary [movement within (axis perpendicular) to the plane] is indicated by the grey
 147 dashed arrows.



148
 149 **Figure 2.** Augite (high Ca-clinopyroxene; $2/m$; unit cell lengths $a = 1.097$, $b = 1$, $c = 0.596$)
 150 crystallographic slip-system signature key (notated as the slip plane and direction) expressed as
 151 the monoclinic crystallographic fundamental sector (lowest form of crystallographic symmetry).
 152 The outer bracketed labels of the key refer to augite's specific crystallographic axis ($\langle a \rangle = [100]$,
 153 $\langle b \rangle = [010]$, and $\langle c \rangle = [001]$). The surrounding diagrams visualise the different slip planes
 154 where the straight black arrows indicate the direction of slip for both twist and tilt boundaries.
 155 For a tilt boundary [movement perpendicular (axis parallel) to the plane] the black arrows also
 156 indicate the tilt axis whereas the plane rotation axis for a twist (*i.e.*, rotating) boundary
 157 [movement within (axis perpendicular) to the plane] is indicated by the grey dashed arrows.

158 Most of the Martian meteorites that are available for study are mafic-ultramafic igneous
159 rocks (Udry et al., 2020) and references therein. To date the Martian meteorites, consist of the
160 clinopyroxene rich shergottites and nakhlites, orthopyroxenite ALH 84001, the dunitic
161 chassignites, and a non-igneous group of polymict breccias. The nakhlites, which are the focus of
162 this study, have average crystal-sizes ranging from 0.29–1 mm with a cumulate texture (Udry &
163 Day, 2018), are ultramafic in composition derived from mafic parental magmas with low-
164 moderate abundances of olivine (1.7–14.9 modal%) and high abundances of augite (55–71
165 modal%; (Udry & Day, 2018). The remaining 0–42 modal% of the nakhlites is mesostasis
166 material (Udry & Day, 2018). The mesostasis material contains varying proportions of
167 clinopyroxene, orthopyroxene, olivine, plagioclase, titanomagnetite, iron sulphides, and glass
168 (Corrigan et al., 2015). The nakhlites are currently considered the largest group of Martian rocks
169 sourced from a singular location on Mars, due to their consistent 10.7 ± 0.8 Ma ejection age
170 (Cohen et al., 2017; Udry et al., 2020). They are also the least affected by shock [*i.e.*, high strain,
171 maximum bulk shock pressures 5–20 GPa (Fritz, Artemieva, et al., 2005)], where shock
172 deformation has been reported to occur as bands within the samples (Daly et al., 2019; Fritz,
173 Artemieva, et al., 2005), potentially leaving regions that are more representative of low strain
174 (mantle) deformation than high strain (shock) deformation. Nearly all of the meteorites within
175 the group contain evidence of aqueous alteration on Mars in the form of iddingsite (Bunch &
176 Reid, 1975; Hallis & Taylor, 2011; Krämer Ruggiu et al., 2020; Lee et al., 2015; Noguchi et al.,
177 2009; Treiman, 2005; Udry et al., 2020), and have been shown to sample several temporally
178 distinct igneous events that are geochemically related by a shared magma source region (Cohen
179 et al., 2017; Day et al., 2018; Treiman, 2005; Udry et al., 2020). Recent specimen additions to
180 the nakhlite group over the last decade have questioned the former hypothesised formation
181 mechanism of the nakhlites [*i.e.*, a large cumulate lava flow on the surface of Mars (Treiman,
182 2005)]. This raises the question as to whether the nakhlites formed solely as lava flows, shallow
183 (≤ 3 km depth) intrusions, or a combination of flows and intrusions.

184 Majority of the work on augite and olivine deformation has been focused on
185 understanding mantle (*i.e.*, low strain rate -low stress – high temperature) conditions. However,
186 due to the mechanism of nakhlite extraction by impact and ejection deformation in these
187 meteorites is expected to contain high strain rate deformation in the form of shock
188 metamorphism. This shock deformation. This shock deformation although reported to be low in
189 comparison to other Martian meteorites (Fritz, Artemieva, et al., 2005), will have impacted and
190 may have overprinted the magmatic deformation signatures within the nakhlites. Accordingly, in
191 principle nakhlites are expected to carry signatures of both emplacement and ejection. This study
192 asks: can crystallographic deformation parameters be used to further the understanding of rocky
193 (planetary) bodies other than Earth, including the Moon, asteroids, and Mars? To tackle this
194 question, crystal plastic deformation (slip-systems) of olivine and clinopyroxene within the
195 nakhlites from Mars are investigated.

196 **2 Materials and Methods**

197 Twenty-one Large Area EBSD datasets were collected for this study, covering 16
198 individual nakhlite meteorites: Caleta el Cobre 022, Governador Valadares, Lafayette, Miller
199 range (MIL) 03346, MIL 090030, MIL 090032, MIL 090136, Nakhla, Northwest Africa (NWA)
200 817, NWA 998, NWA 10153, NWA 11013, NWA 12542, Yamato (Y) 000593, Y 000749, Y
201 000802 (Table 1). The presented EBSD data includes all known ‘paired stones’ for the Miller

202 Range (MIL) and Yamato (Y) nakhlites. Two sections of five meteorites: Governador Valadares,
203 Nakhla, Northwest Africa (NWA) 998, Y 000593, and Y 000749 were also analysed to assess
204 the impact of experimental parameters as well as result consistency across different sections.

205 Each analysed thick section was coated with a ~10 nm thick conductive carbon coat using
206 a sputter coater after undergoing both mechanical (iterative 1 μm followed by 0.3 μm aluminum
207 spheres suspended in glycol for 5 minutes each) and chemical (4 hours using 0.1 μm colloidal
208 silica suspended in a NaOH solution) polishing prior to EBSD analysis.

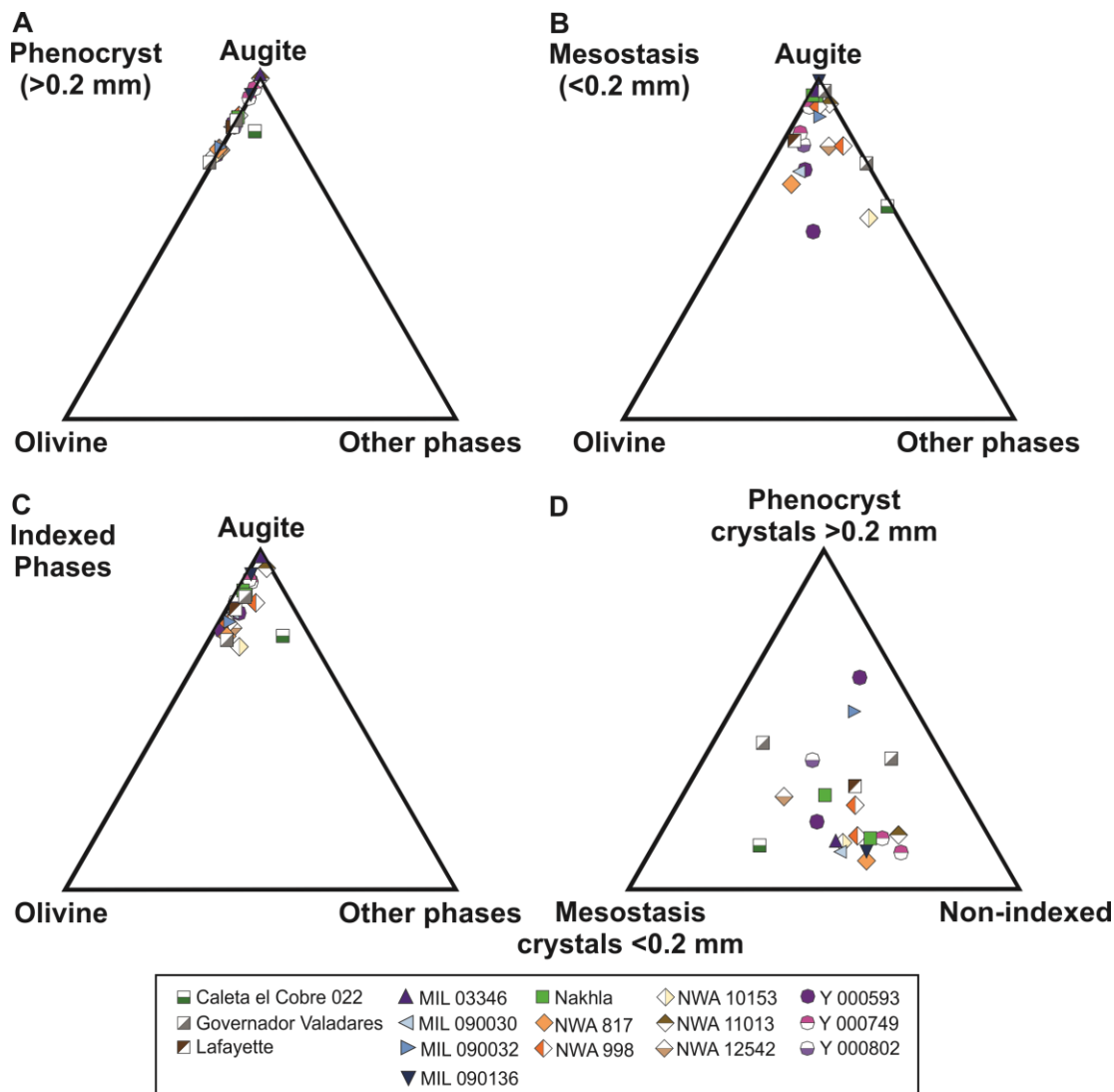
209 EBSD analyses were run using four different instruments in four different labs: ISAAC
210 imaging centre, University of Glasgow (Zeiss Sigma Field Emission Gun Variable Pressure
211 Scanning Electron Microscope (FEG-VP-SEM) with Oxford Instruments NordlysMax² EBSD
212 detector, operating Oxford Instruments AZtec analysis software v3.3); Geochemical Analysis
213 Unit (GAU), Macquarie University (Carl Zeiss IVO SEM using a HKL NordlysNano high
214 Sensitivity EBSD detector); Oxford Instruments Nanoanalysis HQ, High Wycombe (Hitachi
215 SU70 FEGSEM equipped with a Symmetry CMOS detector and indexed using AZtec analysis
216 software v3.4); and the John de Laeter Centre, Curtin University (Tescan MIRA3 VP-FESEM
217 with the NordlysNano EBSD detector and AZtec EDS/EBSD acquisition system). All analyses
218 were run at 20 keV, 4–8 nA beam current, at a 70° tilt, under high vacuum (~3.4 x 10⁸ Pa) apart
219 from MIL 03346 (118) and Lafayette (USNM 1505-1), which were run at low vacuum (~49 Pa).
220 Selected step sizes (ranging 0.4–15 μm) for each sample were chosen to maximise the area
221 covered by the EBSD maps and ensure data collection over available timeframes whilst ensuring
222 the MAD values, indicators of index quality, were <1 (all phases ranging 0.48–0.82; Table 1).

223 All EBSD datasets were processed using Oxford Instruments Channel 5 software.
224 Crystallographic axes for the forsterite and augite phases were defined as $b = 1 > c = 0.587 > a =$
225 0.466 (forsterite) and $a = 1.097 > b = 1 > c = 0.596$ (augite). To remove erroneous data (i.e., mis-
226 indexed and non-indexed data points) without generating significant artefacts within the datasets
227 (Bestmann and Prior, 2003; Watt et al., 2006; Forman et al., 2016; Daly et al., 2019a; Forman et
228 al., 2019) the data was first noise reduced using a wildspike correction followed by a consecutive
229 8–6 point nearest neighbour zero solution reductions. Crystal boundaries were defined as >10°
230 internal crystallographic misorientation from the nearest-neighbour pixel. Mechanical twins were
231 identified as 180° rotation around augite (100), (204), or (104) axes and 60° rotation around
232 forsterite (011), (012), and (100) axes. Simple twin boundaries were also identified in augite as
233 180° rotation around augite (001).

234 Meteorites, such as the nakhlites presented here, lack any consistent external reference
235 frame. Principal orientations have therefore been arbitrarily defined as Y = top–bottom direction
236 of the thick section's polished surface, X = left–right direction of the thick section's polished
237 surface, and Z = direction perpendicular to the plane of the thick section's polished surface.
238 EBSD is a reference-frame based technique thus, assigning a pseudo-external reference frame for
239 the samples will enable comparison across the samples and provide a semblance of consistency
240 in the analysis across all of the datasets. Grain (i.e., crystal) reference orientation distribution
241 (GROD) angle maps were used to identify regions of high deformation and low deformation
242 within each of the nakhlites. Once the identified regions were checked against local
243 misorientation, inverse pole figure (IPF), Euler, and phase maps specific subsets were created.
244 All slip-system diagrams [misorientation axis inverse pole figure (mIPF) plots] for high

245 deformation, low deformation, and whole section datasets have been contoured using the settings
 246 of a maximum multiple uniform density (MUD.; representing the density of data points) of 5
 247 with 5° clustering and a half width of 15° for internal misorientation between adjacent pixels
 248 ranging 2–10°. Slip-systems present within each dataset were identified from the MUD
 249 distribution patterns within the mIPF plots.

250 3 Results



251
 252 **Figure 3.** Compositional breakdown of EBSD datasets for analysed nakhlite samples. A)
 253 compositional breakdown of indexed phenocrysts (>0.2 mm crystals). A higher proportion of
 254 other phases is observed within Caleta el Cobre 022 reflecting the increased abundance of
 255 plagioclase within the sample. B) Compositional breakdown of indexed mesostasis (<0.2 mm
 256 crystals) C) Compositional breakdown of all indexed phases (phenocrysts and mesostasis). D)
 257 Distribution between phenocrysts crystals (>0.2 mm), mesostasis crystals (<0.2 mm), and non-
 258 indexed portions (representing the combination of voids, glass, and amorphous phases) of the
 259 large area EBSD maps. For a full breakdown of indexed phases, the reader is referred to the
 260 supplementary Table A1 and Figure A1.

261 3.1 Naxhlite Modal Mineralogy

262 Augite is observed as the dominant phase {29.2 vol% [Y 000749 (72-A)] to 66.0 vol.%
 263 [Nakhla (WAM 12965)]} in all collected datasets with variable proportions of olivine {0.3 vol.%
 264 (MIL 03346 and NWA 11013) to 14.9 vol.% [Y 000593 (127-A)]; Fig. 3}. The mineralogy is
 265 observed to be heterogeneously dispersed with pockets of increased mesostasis abundance {10
 266 vol.% [Y 000593 (127-A)] to 60 vol.% (Caleta el Cobre 022)} relative to phenocrysts {9 vol.%
 267 NWA (817) to 62 vol.% [Y 000593 (127-A)]; Fig. 3}.

269 3.2 Identification of naxhlite high and low deformation regions

270 Assessment of combined augite and olivine mIPF major slip-system patterns for all
 271 twenty-one analysed naxhlite sections reveal nine distinct groupings (Fig. 4). These nine groups
 272 are the culmination of both high and low strain deformation within the samples. However,
 273 GROD angle maps of the sections show defined regions of high and low deformation (*e.g.*, Fig.
 274 5). GROD maps are used to assess bending (*i.e.*, plastic deformation) within a given crystal. Here
 275 the average orientation of a crystal is chosen as a fixed reference point and the amount of
 276 deviation in orientation is depicted from blue [0 (*i.e.*, same orientation)] through to red [10°
 277 deviation (*i.e.*, the determined cutoff for a grain boundary)]. Thus, within the GROD angle map
 278 blue crystals indicate no bending within the crystal [interpreted as low strain (L)] and regions of
 279 yellowish-green through to red depict bent regions within the crystal [interpreted as high strain
 280 (H)]. In figure 5, and other analysed sections (Figs. 6–13), high strain regions are observed to
 281 form as bands. These bands are typically located in mesostasis-rich and glass-rich regions, where
 282 the associated phenocrysts often exhibit increased density of fractures, and irregular linear
 283 features that do not produce diffraction patterns higher, as well as mechanical twins (white
 284 bands).

285 Out of the 21 analysed sections, both NWA 10153 and NWA 11013 (Fig. 7) exhibit
 286 significantly less areas of low deformation (<2° GROD angles). In these sections the distribution
 287 of the higher deformation regions is observed to be more ubiquitous throughout the map area
 288 (Fig. 7). Section Y 000593 (127-A) on the other hand, shows minimal internal deformation
 289 relative to the other analysed sections, including its replicate section Y 000593 (106-A). Majority
 290 of the analysed crystals within the section exhibit GROD angles <1°, where the highest GROD
 291 angle observed is observed at <5° and restricted to smaller fractured crystals (Fig. 13).

292 Within the analysed naxhlites, augite exhibits two types of twins: simple twins (grey lines
 293 depicting 180° rotation about the {001} axis in augite) and mechanical twins (white lines
 294 representing the rotation of 180° and 60° around the {100} axis in augite and olivine,
 295 respectively). The simple twins are observed throughout the various analysed sections appearing
 296 in both low and high deformation regions (Fig. 5–13). The mechanical twins, however, only
 297 appear in high deformation regions (*e.g.*, Figs 5 and 7). The mechanical twins appear with
 298 noticeable chevron patterns within augite crystals with higher GROD angle values or crystals on
 299 the boundary of regions of increased angle misorientation, particularly within samples Caleta el
 300 Cobre 022 (Fig. 5), Governador Valadares (BM.1975,M16,P8469), Lafayette, MIL 03346, MIL
 301 090032 (Fig. 6), NWA 817, NWA 10153, NWA 11013 (Fig. 7), NWA 12542, and Y 000593
 302 (106-A). The mechanical twins are observed to span either the width of the crystal or where

303 simple twinning is also present (occurring along the {001} axis in augite) the mechanical twins
 304 form from the edge of the crystal into the simple twin boundary (light grey lines). Simple twins
 305 observed in augite appear throughout the sections appearing in both high and low deformation
 306 designated regions (Fig. 5-13).

307 Investigation of augite and olivine mIPF slip-system patterns for the depicted H and L
 308 regions within each analysed section (*e.g.*, Figs. 5–13), reveal shifts in the observed patterns
 309 (Figs. 14 and 15, Table 2). Overall, the dominant slip-system patterns identified in the H regions
 310 match those of the overall section slip-system patterns (Figs 13 and 14, Table 2) depicting nine
 311 different groups. However, changes in the pattern intensity and secondary slip-system patterns
 312 are observed (*e.g.*, Fig. 5). Within olivine (forsterite) mIPF plots (010)[001] combined with
 313 {hk0}{001} is observed as the most common slip-system pattern for nakhlite olivine [Group I (5
 314 meteorites): Caleta el Cobre 022, Governador Valadares, Lafayette, NWA 12542, and Y 000593
 315 (Fig. 4 and 13)]. Note that due to the low modal abundance of olivine within the samples overall
 316 (0.3–14.9 vol.%; Fig. 3) the number of crystals contributing to the observed crystallographic
 317 dislocations are far below those recommended for statistically relevant and whole-rock
 318 representative results (5–84 crystals, *i.e.*, <100 crystals; Watt et al., 2006) with the exception of
 319 NWA 12542 *F83-1* (136 crystals; Figs. 3–13). Overall, five unique olivine slip-system patterns
 320 [{hk0}, (010)[001], (010)[100]+(010)[001], (001)[100]/(100)[001], (010)[001]+{hk0}] are
 321 observed across the analysed samples where the overriding slip-system becomes clearly defined
 322 from the minor slip-systems with increased crystal count (Fig. 14).

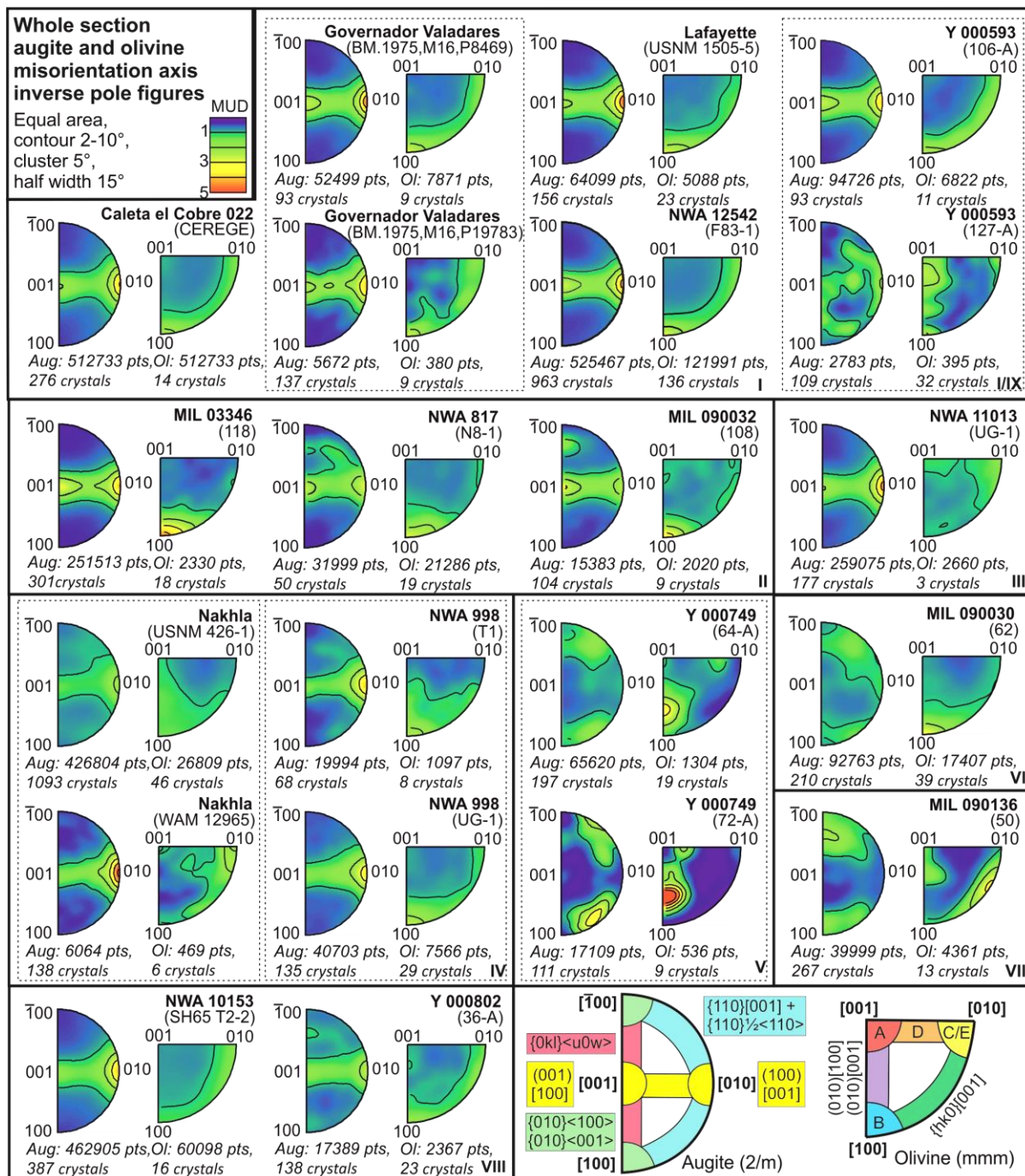
323 For augite, 16 sections out of the 21 EBSD individual scans had statistically relevant
 324 datasets (>100 crystals; Watt et al., 2006) only 5 datasets contained <100 crystals [Governador
 325 Valadares (BM1975,M16,P8469), MIL 090032 (62; Fig. 5), NWA 817 (N8-1), NWA 998 (T1;
 326 Fig. 7), and Y 000593 (106-A); Figs. 3–5]. For augite four distinct mIPF slip-system patterns are
 327 identified with the two most commonly observed slip-system patterns involving the pairing of
 328 (100)[001] (major) and (001)[100] (minor) dislocations expressed at varying proportions (groups
 329 I–III, VIII; Fig. 14). Within Figure 14, groups I and II exhibit a higher proportion of (001)[100]
 330 dislocations compared to groups III and VIII (*e.g.*, Figs. 5–7, and 12, respectively). Augite
 331 {110}[001] + {110} $\frac{1}{2}$ <110> slip-system dislocations are also observed in groups V and VI,
 332 (010)[100]+(010)[001] slip-system dislocations in group VII (MIL 090136; Fig. 11), and a
 333 combination of multiple slip-systems, including components of (100)[001], (001)[100],
 334 {0kl}<u0w>, {110}[001] + {110} $\frac{1}{2}$ <110>, within Y 000593 (section 127-A; Figs. 13 and 14).

335 When assessing the identified L regions mIPF dominant slip-system patterns were
 336 observed to shift but only for certain analysed sections [*i.e.*, sections relating to nakhlites Caleta
 337 el Cobre 022 (Fig. 5), NWA 817, NWA 11013 (Fig. 7), Nakhla, MIL 090030 (Fig. 10), MIL
 338 090136 (Fig. 11), Y 000802 (Fig. 12), and Y 000593 (Fig. 13)]. Out of the nine identified high
 339 deformation region groups, excepting group V, at least one analysed section exhibited different
 340 low deformation region mIPF slip-system patterns (Table 2, Figs. 14 and 15). For the sections
 341 that showed different slip-system patterns between the H and L regions, pattern shifts were often
 342 only observed to occur in either olivine and augite, where olivine is the more likely mineral to
 343 exhibit a shift (Fig. 15, Table 2). However, additional shifts in mIPF slip-system patterns and
 344 intensity can also be observed as additional slip-systems patterns within the L region mIPFs even
 345 when the major slip-system pattern remains the same (Fig. 15). All L region mIPF slip-system
 346 patterns appear unique to the individual meteorite. More importantly, different low deformation

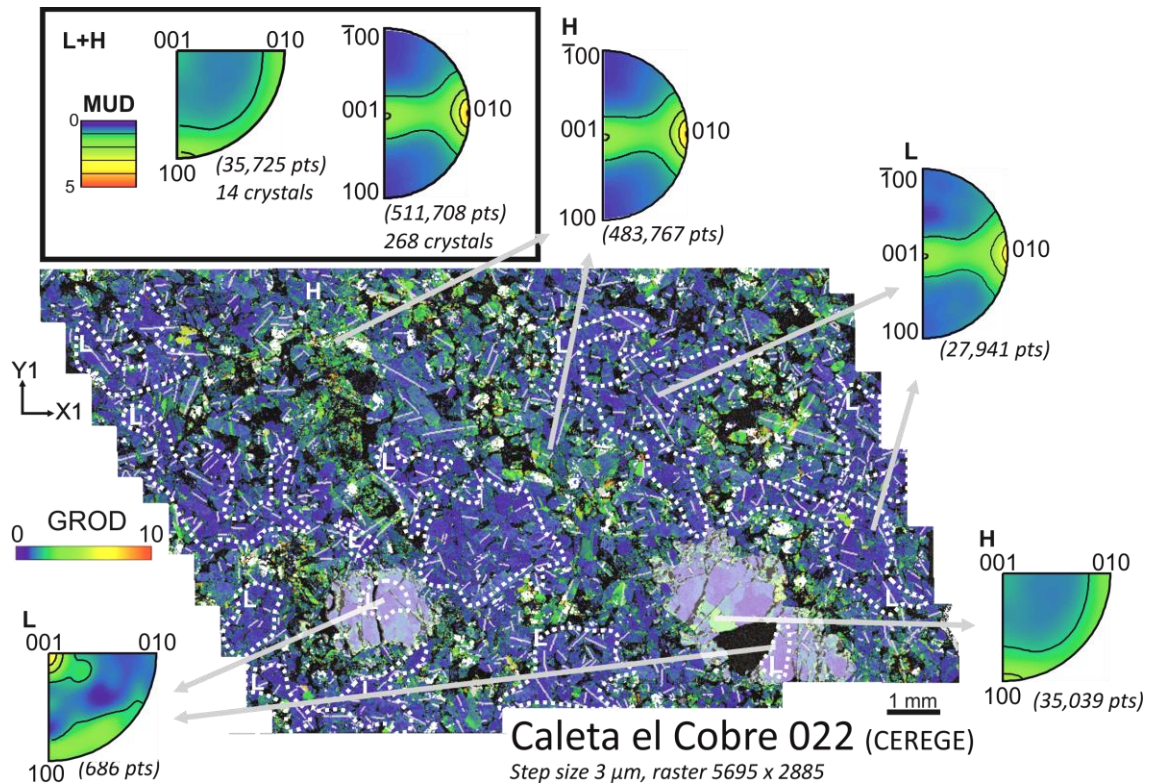
347 mIPF slip-system patterns are observed to occur within group II (Table 2, Fig. 15), where
348 meteorites MIL 03346 and NWA 817 exhibit the same H region mIPF slip-system patterns but
349 distinct L region mIPF patterns (Figs. 14 and 15, Table 2). This indicates that the cause of the H
350 region mIPF slip-system patterns most likely independent of the L region mIPF slip-system
351 patterns.

352 In order to assess consistency in the presented analysis replicate sections were run for
353 five of the sixteen analysed nakhlites. In these replicate sections, the same major augite and
354 olivine mIPF slip-system patterns (both H and L region) are expressed for the meteorites
355 Governador Valadares, NWA 998, and Y 000749. However, discrepancies in olivine slip-system
356 patterns are observed between the two Nakhla sections {USNM 426-1 exhibiting (010)[001] H
357 region patterns and WAM 12965 exhibiting (001)[100]/(100)[001] H region patterns} as well as
358 differences in both augite and olivine slip-system patterns between the two Y 000593 sections
359 {106-A exhibiting dominant (100)[001] with minor (001)[100] for augite and (010)[001] with
360 {hk0}[001] for olivine and section 127-A exhibiting multiple dislocations in augite and
361 (010)[100]+(010)[001] for olivine}. Furthermore, low amounts of internal misorientation are
362 observed within the GROD angle map (Fig. 13). 120° triple junctions (typical annealing textures)
363 are also observed within Y 000593 (127-A)'s clustered olivine within which were not identified
364 within Y 000593 (106-A). The observed variability of slip-system patterns within Nakhla and Y
365 000593 meteorites have direct implications for methodological parameters *e.g.*, step-size and
366 number of assessed crystals, textural heterogeneity, *etc.* which will be further evaluated in the
367 discussion.

368

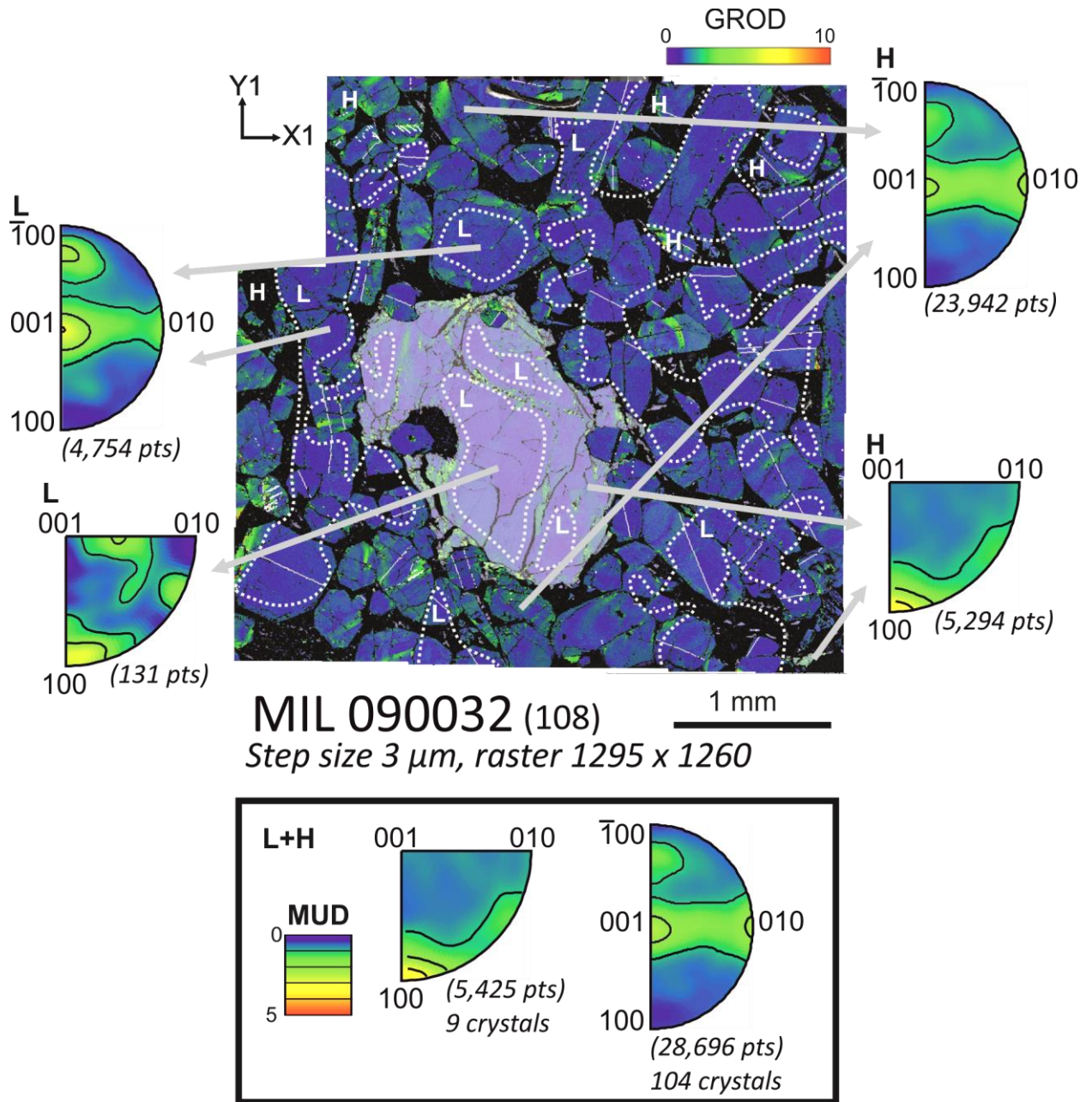


369
 370 **Figure 4.** Misorientation axis inverse pole figure plots (mIPF) for nakhlite whole section data.
 371 Augite (half-circles) and olivine (quarter circles) represented as their fundamental sectors (lowest
 372 form of crystal symmetry) where the misorientation is referenced against the crystal co-ordinate
 373 system. We identify 8 (potentially 9) different major slip system combinations for the nakhrites
 374 based on their respective keys (bottom right box) where each colour indicates a different type of
 375 dominant slip-system. Olivine key: A = (010)[100], B = (010)[001], C = (100)[001], D =
 376 {0kl}[100], E = (001)[100].

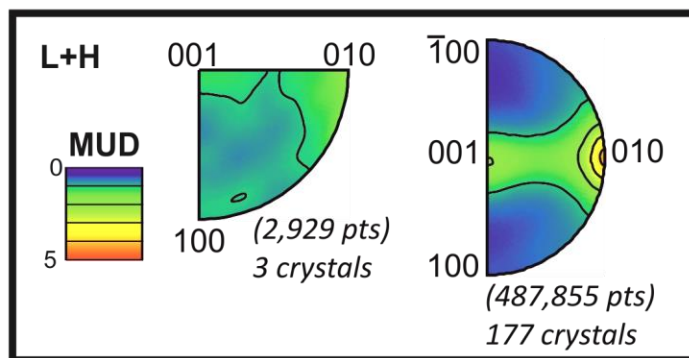
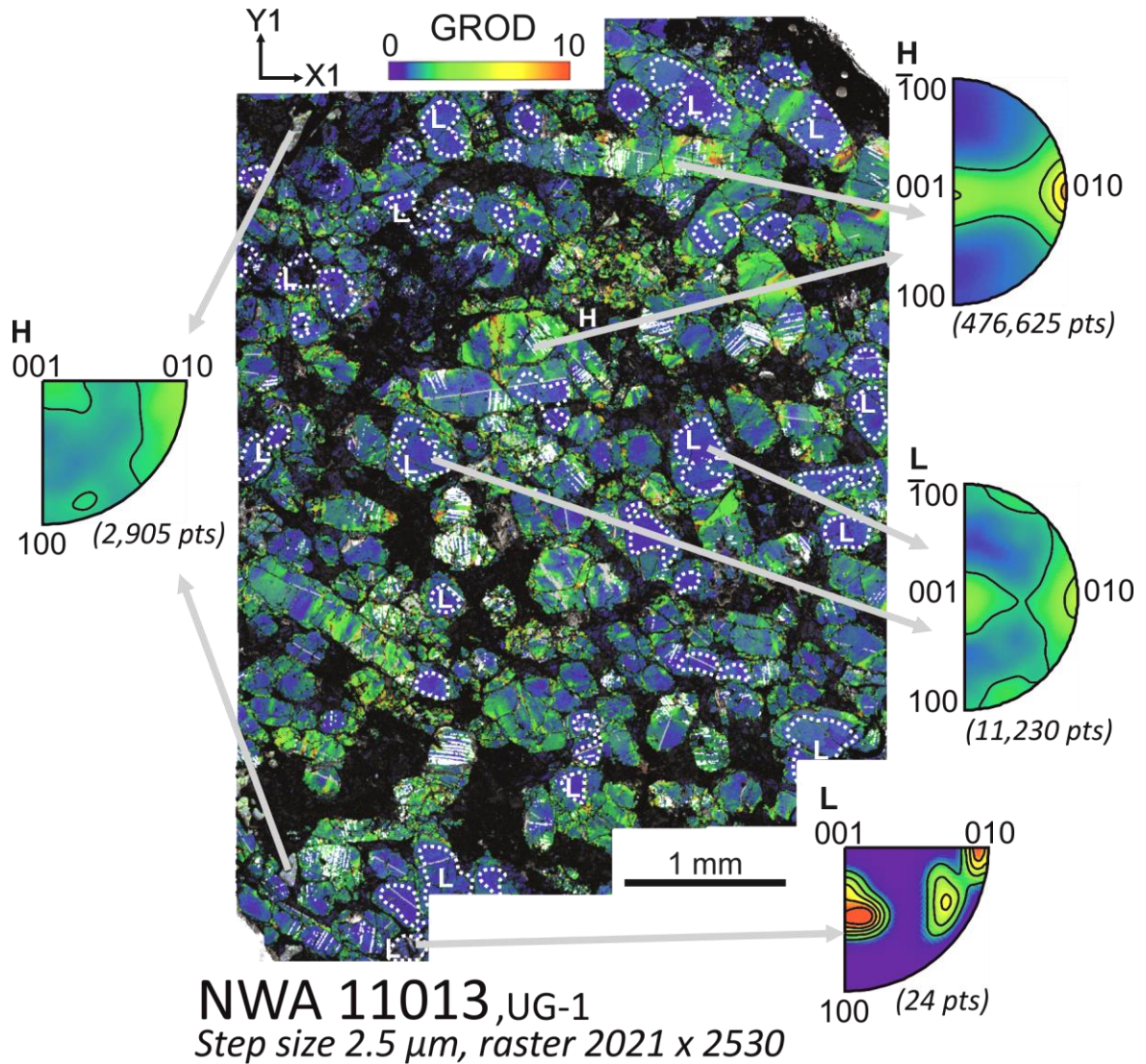


378
 379
 380
 381
 382
 383
 384
 385
 386
 387
 388
 389
 390
 391
 392

Figure 5. Grain relative orientation (GROD) angle map (0–10°) Caleta el Cobre 022 (group I) with augite and olivine misorientation axis inverse pole figures (mIPF)s for low deformation regions (L), high deformation regions (H), and whole section representative slip-system signatures (L+H). Combined slip-system signature is dominated by high deformation signature. Between L and H mIPFs, a shift is observed in olivine signature while augite signatures remain constant. The GROD map depicts the changes in crystallographic orientation within a given crystal between 0–10° relative to the average crystallographic orientation of the crystal. Higher internal misorientations 3–10° angles are observed as green-red regions in each section. These bands of higher internal misorientation align with regions of increased mesostasis abundance. Augite and olivine mechanical twins [white lines; {100} axis in augite (180° rotation) and olivine (60° rotation)], and regions of higher fracture density. Augite simple twins (light grey lines, 180° rotation about {001} axis) an indicator of shock deformation appear throughout both the high and lower misorientation regions. Olivine within the sample is indicated by the white transparent layer.

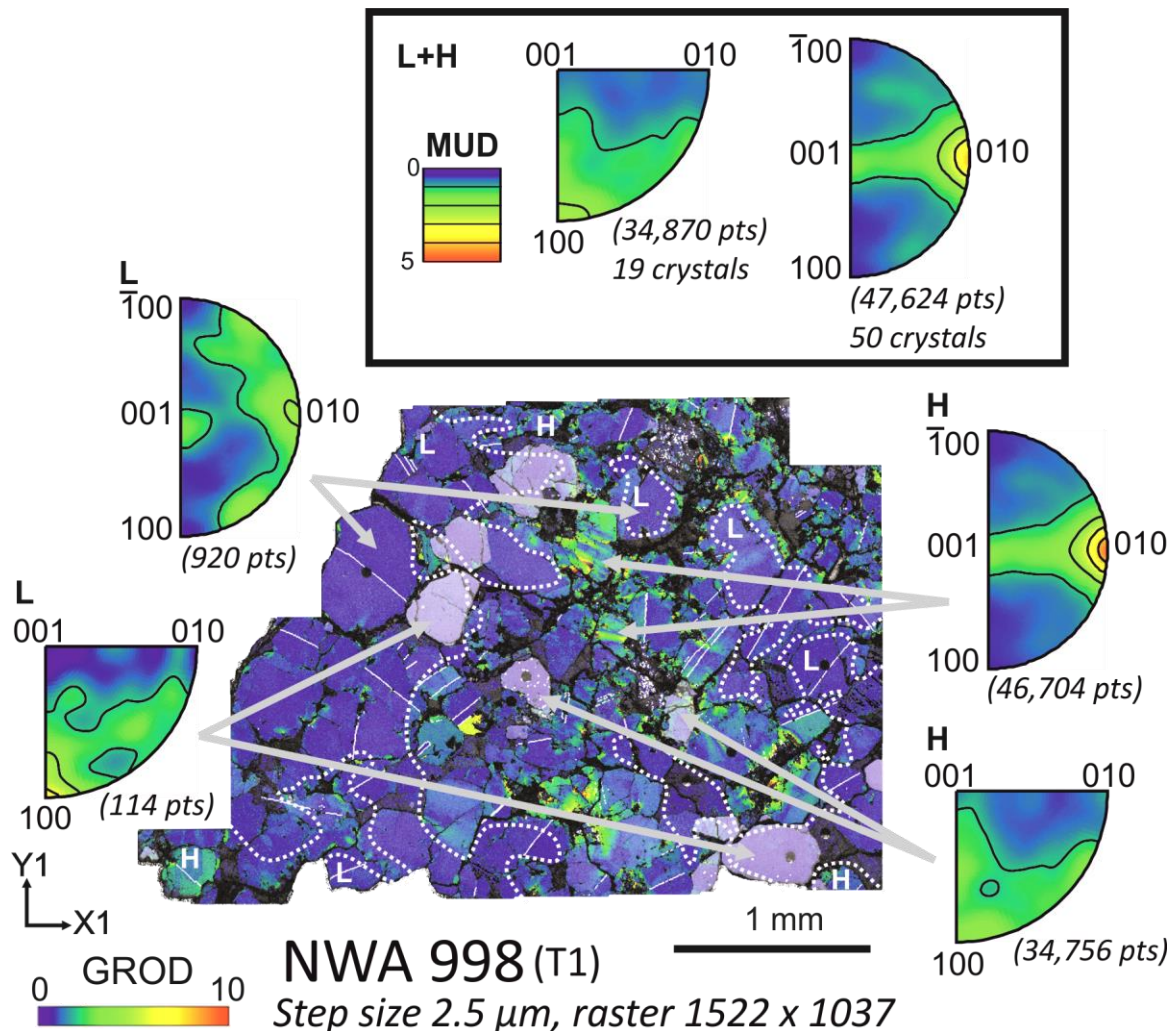


393
 394 **Figure 6.** GROD angle map (0–10°) of MIL 090032 (group II with augite and olivine mIPFs for
 395 low deformation regions (L), high deformation regions (H), and whole section representative
 396 slip-system signatures (L+H). From the mIPF plots signatures from the high deformation regions
 397 (H) are seen to dominate the whole section signature. Between L and H mIPFs a subtle shift in
 398 signature is observed within augite and a significant shift is observed in olivine. In the GROD
 399 angle map bands of higher internal misorientation align with regions of increased mesostasis
 400 abundance. Augite and olivine mechanical twins [white lines; {100} axis in augite (180°
 401 rotation) and olivine (60° rotation)], and regions of higher fracture density. Augite simple twins
 402 (light grey lines, 180° rotation about {001} axis) an indicator of shock deformation appear
 403 throughout both the high and lower misorientation regions. Olivine within the sample is
 404 indicated by the white transparent layer.

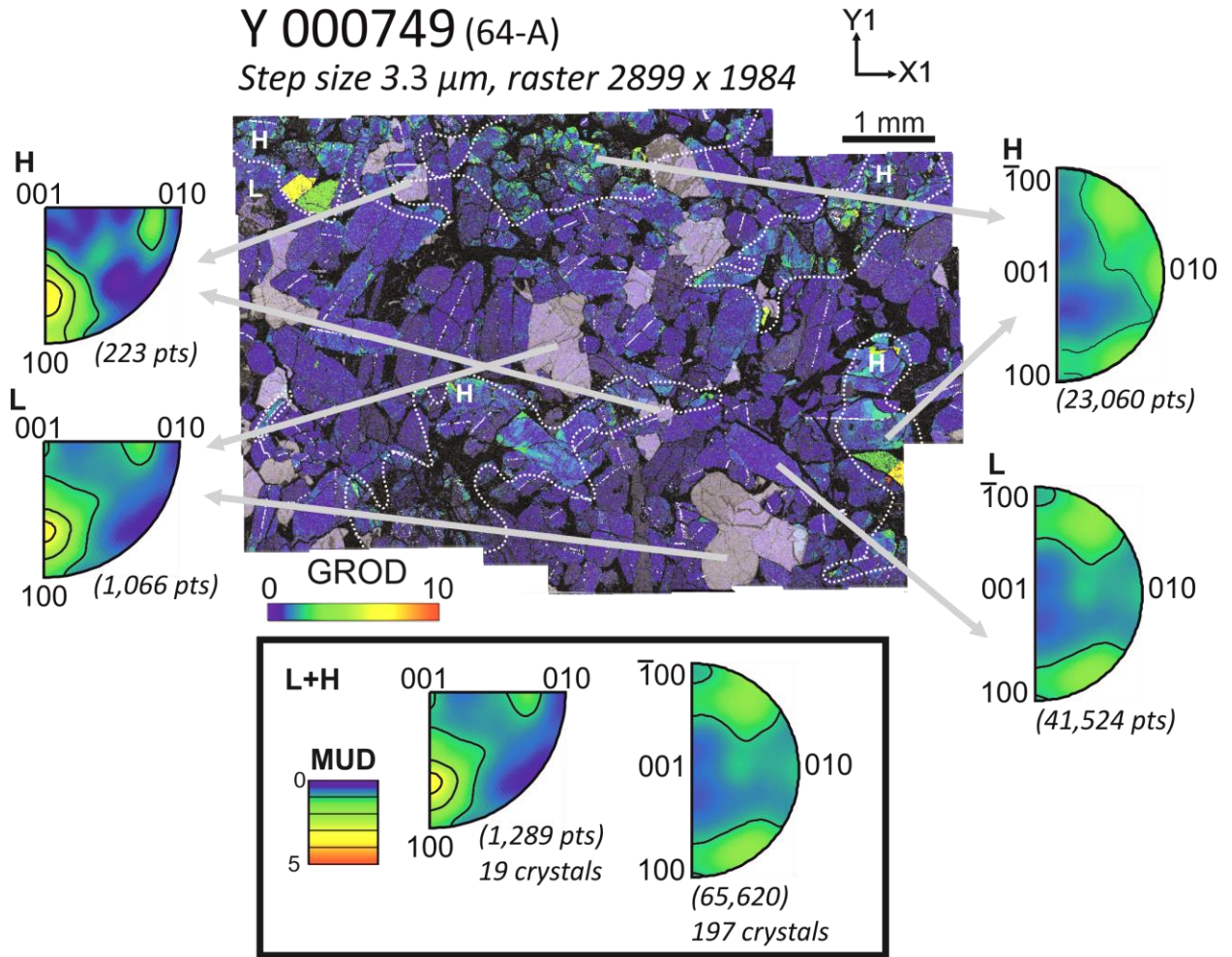


405
406 **Figure 7.** GROD angle map (0–10°) of NWA 11013 (group III) with augite and olivine mIPFs
407 for low deformation regions (L), high deformation regions (H), and whole section representative
408 slip-system signatures (L+H). Whole section signatures are dominated by H signatures. A region
409 signatures show a combination of L region as well as potential low strain slip-systems. In the
410 GROD angle map bands of higher internal misorientation align with regions of increased
411 mesostasis abundance. Augite and olivine mechanical twins [white lines; {100} axis in augite

412 (180° rotation) and olivine (60° rotation)], and regions of higher fracture density. Augite simple
 413 twins (light grey lines, 180° rotation about {001} axis) an indicator of shock deformation appear
 414 throughout both the high and lower misorientation regions. Olivine within the sample is
 415 indicated by the white transparent layer.

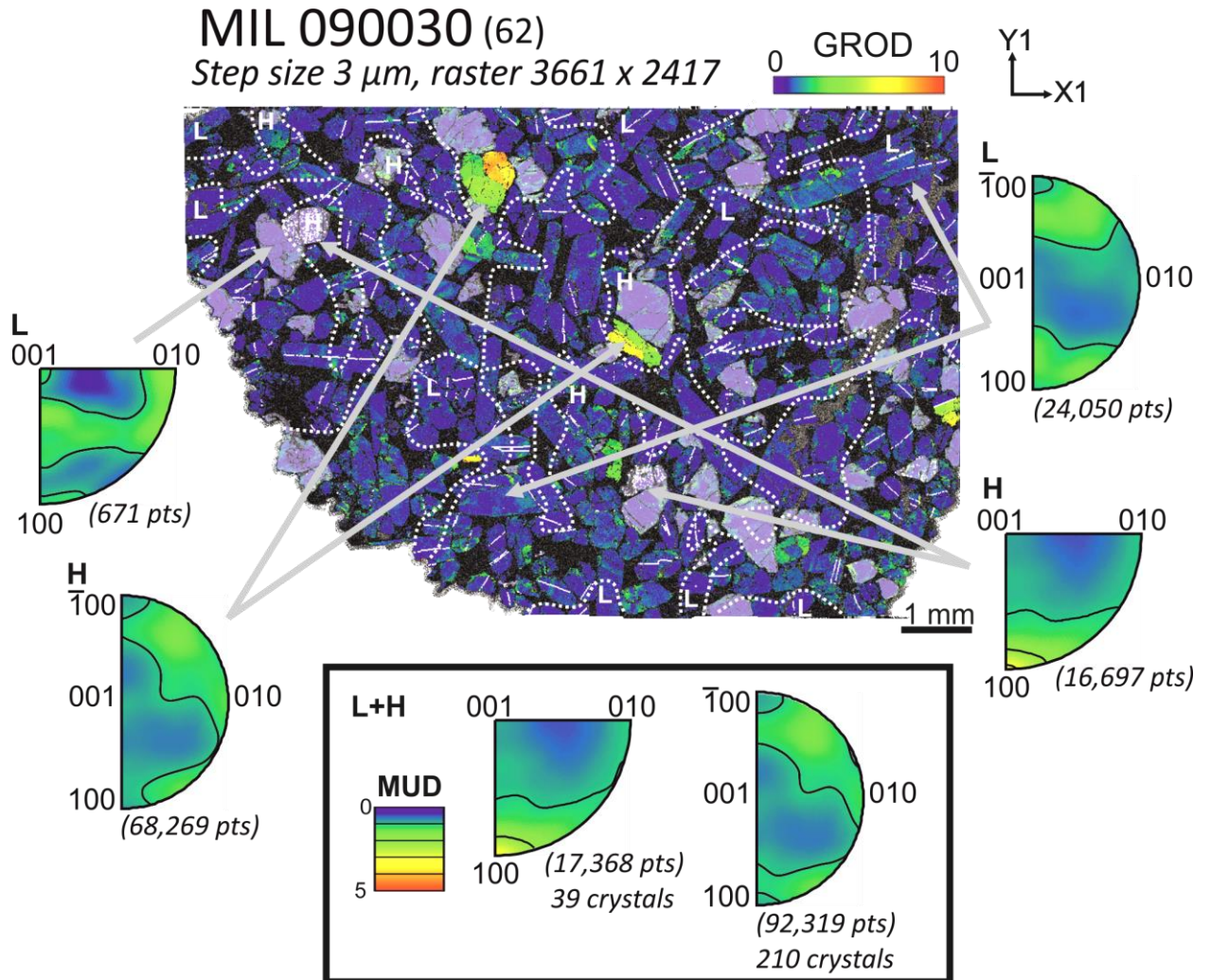


416 **Figure 8.** GROD angle map (0–10°) of NWA 998 (T1; group IV with augite and olivine mIPFs
 417 for low deformation regions (L), high deformation regions (H), and whole section representative
 418 slip-system signatures (L+H). No shift is observed between olivine L and H region signatures
 419 while augite shows a shift in slip-system pattern dominance between the L and H regions. In the
 420 GROD angle map bands of higher internal misorientation align with regions of increased
 421 mesostasis abundance. Augite and olivine mechanical twins [white lines; {100} axis in augite
 422 (180° rotation) and olivine (60° rotation)], and regions of higher fracture density. Augite simple
 423 twins (light grey lines, 180° rotation about {001} axis) an indicator of shock deformation appear
 424 throughout both the high and lower misorientation regions. Olivine within the sample is
 425 indicated by the white transparent layer.



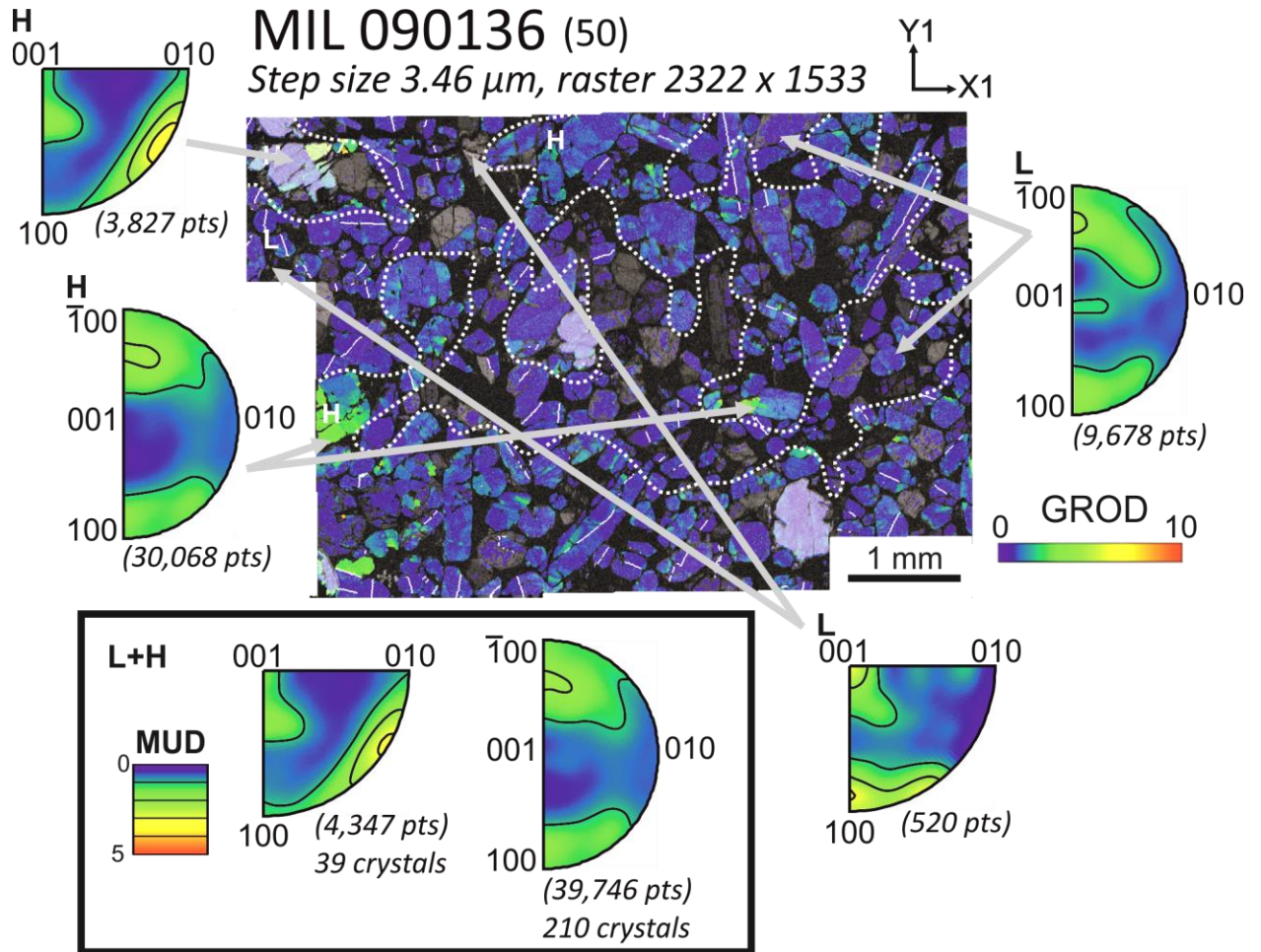
428
 429
 430
 431
 432
 433
 434
 435
 436
 437

Figure 9. GROD angle map (0–10°) of Y 000749 (64-A; group V) with augite and olivine mIPFs for low deformation regions (L), high deformation regions (H), and whole section representative slip-system signatures (L+H). No difference is observed between L and H region slip-system patterns. In the GROD angle map bands of higher internal misorientation align with regions of increased mesostasis abundance. Augite and olivine mechanical twins [white lines; {100} axis in augite (180° rotation) and olivine (60° rotation)], and regions of higher fracture density. Augite simple twins (light grey lines, 180° rotation about {001} axis) an indicator of shock deformation appear throughout both the high and lower misorientation regions. Olivine within the sample is indicated by the white transparent layer.

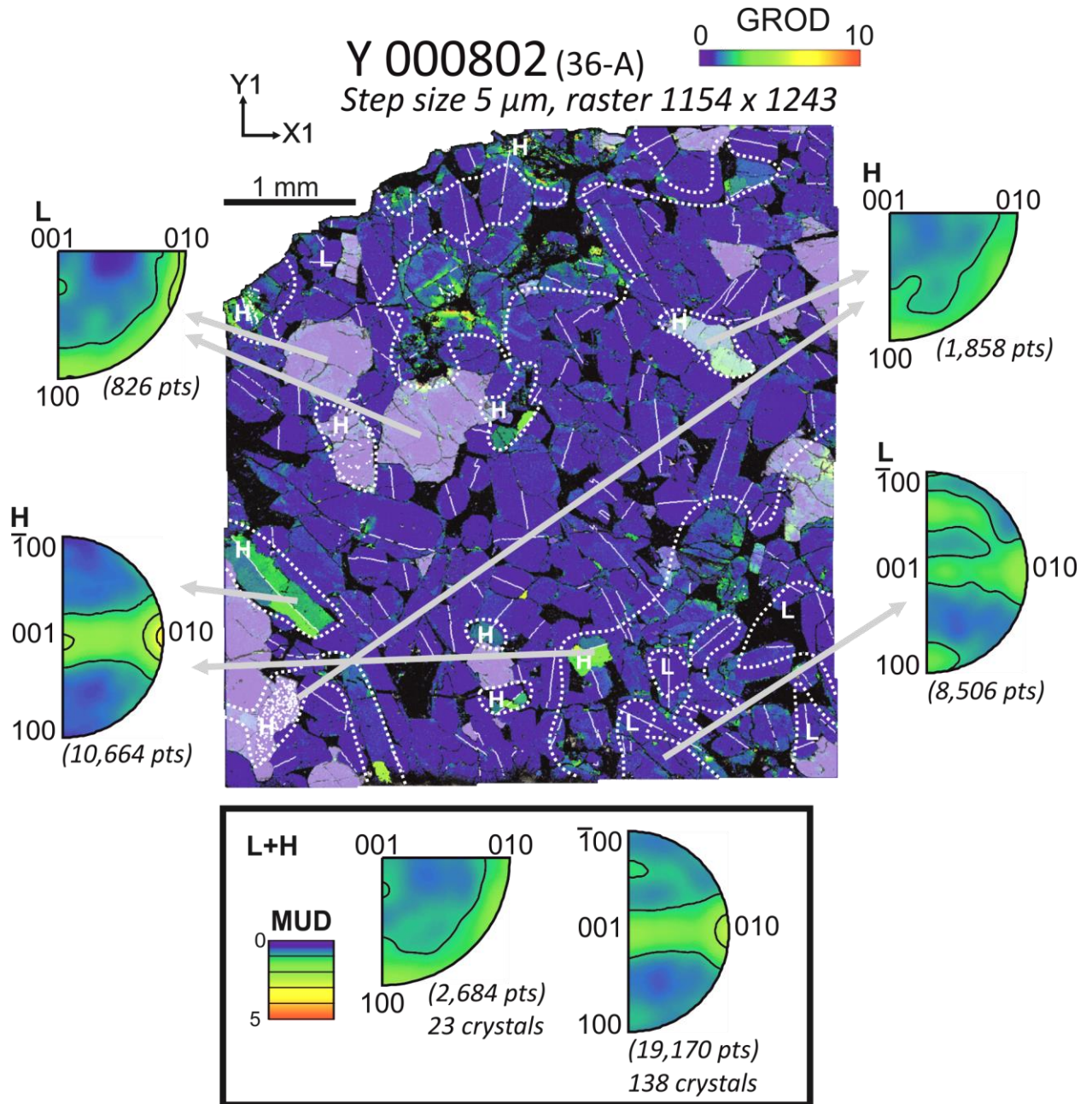


438
 439 **Figure 10.** GROD angle map ($0\text{--}10^\circ$) of MIL 090030 (group VI) with augite and olivine mIPFs
 440 for low deformation regions (L), high deformation regions (H), and whole section representative
 441 slip-system signatures (L+H). H region patterns dominate the whole system patterns. A shift in
 442 slip-system pattern is observed between the low and high deformation regions for both augite
 443 and olivine. In the GROD angle map bands of higher internal misorientation align with regions
 444 of increased mesostasis abundance. Augite and olivine mechanical twins [white lines; $\{100\}$ axis
 445 in augite (180° rotation) and olivine (60° rotation)], and regions of higher fracture density.
 446 Augite simple twins (light grey lines, 180° rotation about $\{001\}$ axis) an indicator of shock
 447 deformation appear throughout both the high and lower misorientation regions. Olivine within
 448 the sample is indicated by the white transparent layer.

449

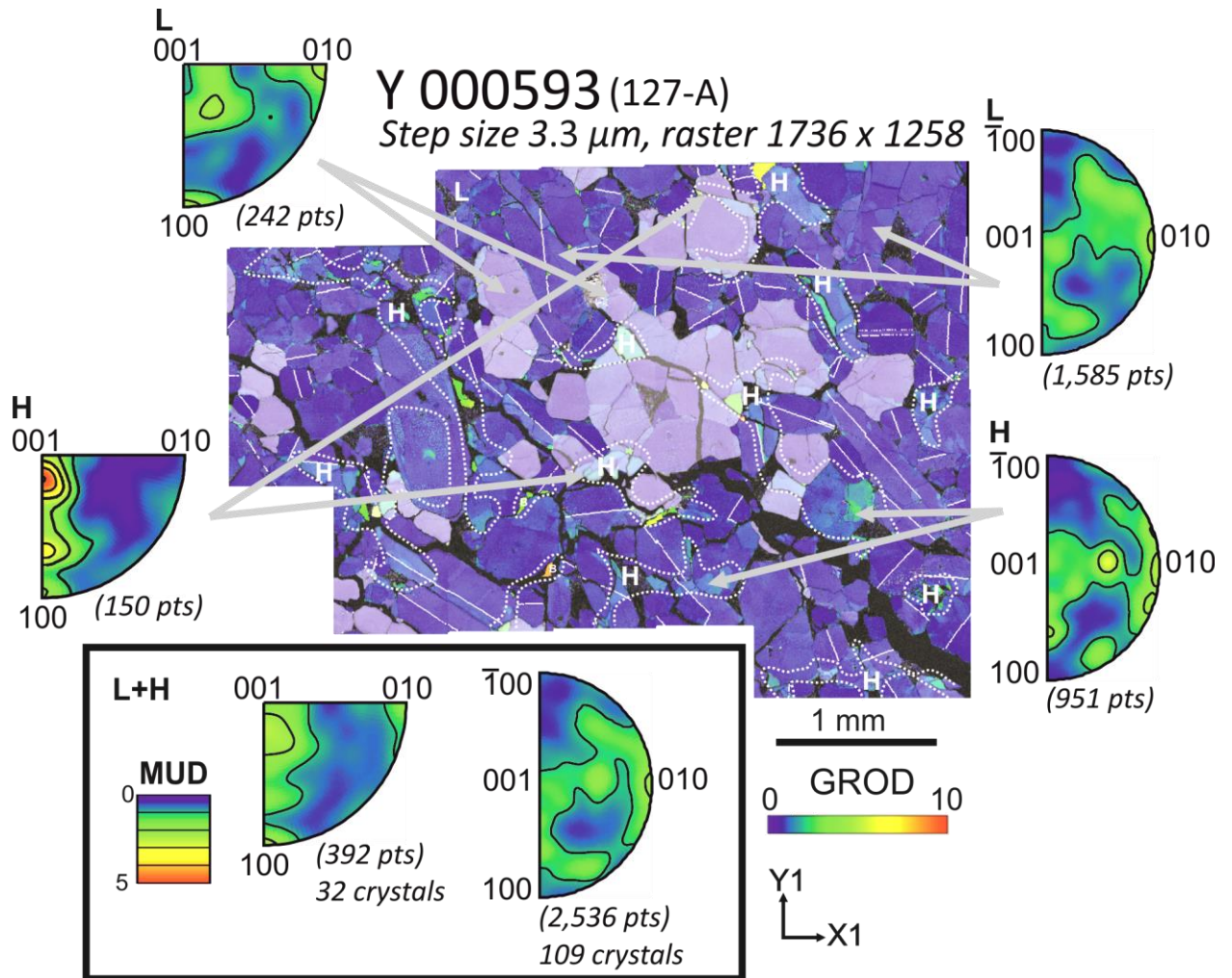


450
 451 **Figure 11.** GROD angle map (0–10°) of MIL 0901362 (group VII) with augite and olivine
 452 mIPFs for low deformation regions (L), high deformation regions (H), and whole section
 453 representative slip-system signatures (L+H). A slight shift in slip-system pattern is observed
 454 within olivine between high and low deformation regions with little change observed in augite.
 455 Overall slip-system patterns from the high deformation regions are observed to dominate the
 456 expressed slip-system patterns for the overall scan. In the GROD angle map bands of higher
 457 internal misorientation align with regions of increased mesostasis abundance. Augite and olivine
 458 mechanical twins [white lines; {100} axis in augite (180° rotation) and olivine (60° rotation)],
 459 and regions of higher fracture density. Augite simple twins (light grey lines, 180° rotation about
 460 {001} axis) an indicator of shock deformation appear throughout both the high and lower
 461 misorientation regions. Olivine within the sample is indicated by the white transparent layer.



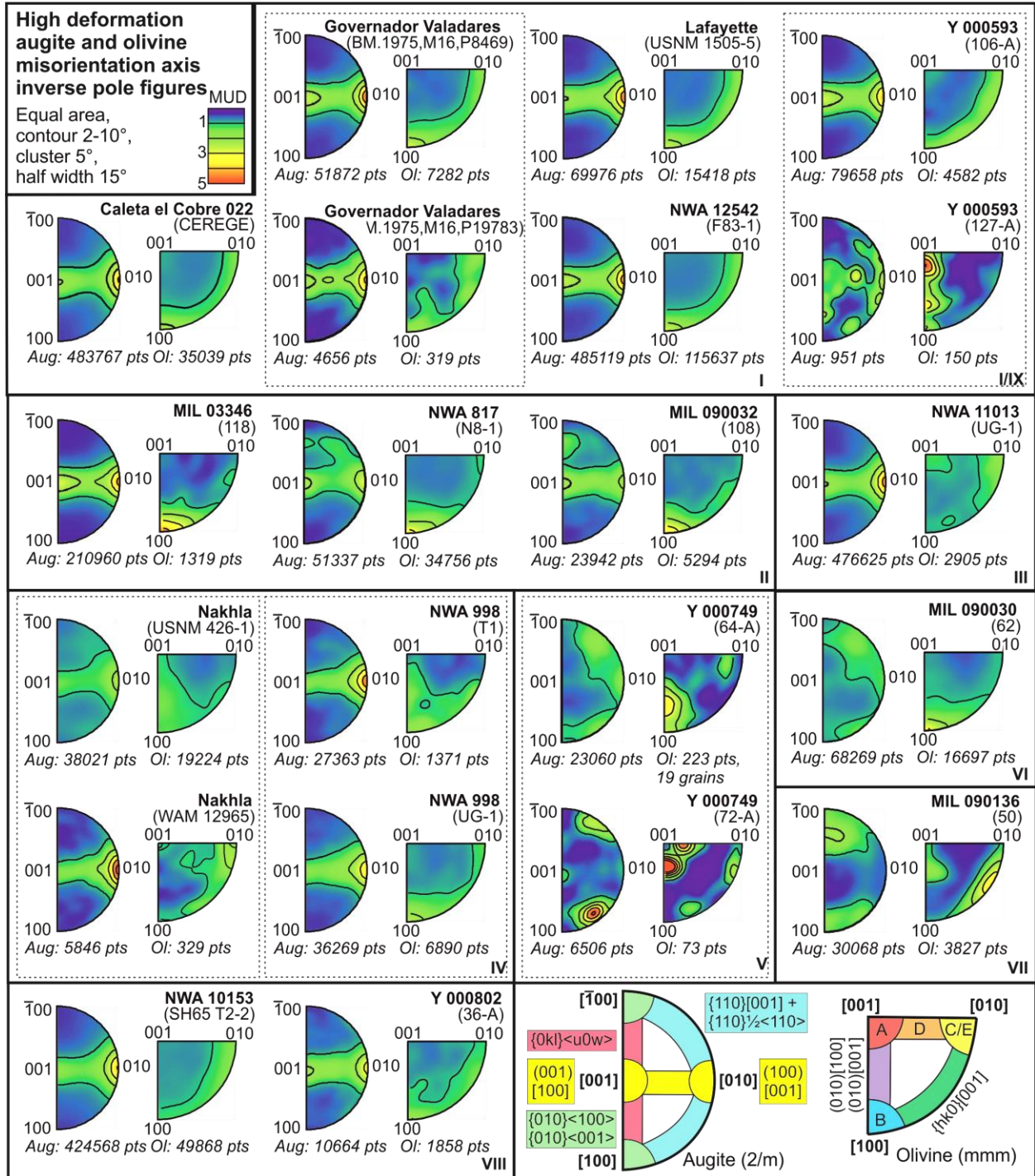
463
 464 **Figure 12.** GROD angle map (0–10°) of Y 000802 (group VIII) with augite and olivine mIPFs
 465 for low deformation regions (L), high deformation regions (H), and whole section representative
 466 slip-system signatures (L+H). Whole scan slip-system patterns show a high influence from the
 467 high deformation regions with some contribution from the low deformation regions. For the low
 468 deformation slip-system patterns, additional patterns are observed within the low deformation
 469 augite as well as olivine indicating potential mantle deformation in combination with shock. In
 470 the GROD angle map bands of higher internal misorientation align with regions of increased
 471 mesostasis abundance. Augite and olivine mechanical twins [white lines; {100} axis in augite
 472 (180° rotation) and olivine (60° rotation)], and regions of higher fracture density. Augite simple
 473 twins (light grey lines, 180° rotation about {001} axis) an indicator of shock deformation appear

474 throughout both the high and lower misorientation regions. Olivine within the sample is
 475 indicated by the white transparent layer.



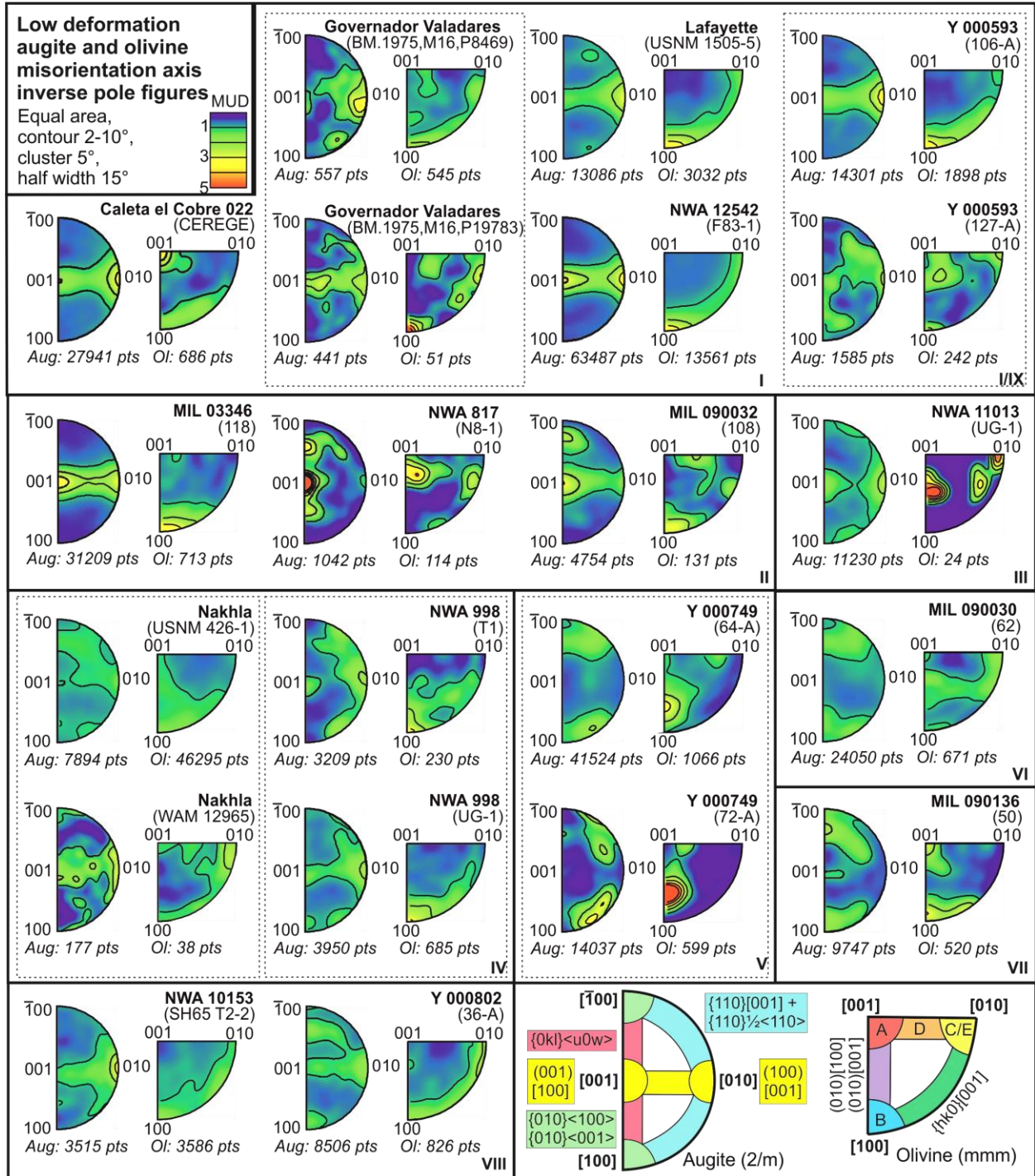
476
 477 **Figure 13.** GROD angle map (0–10°) of Y 000593 (group IX) with augite and olivine mIPFs for
 478 low deformation regions (L), high deformation regions (H), and whole section representative
 479 slip-system signatures (L+H). A shift in slip-system pattern is observed between the high and
 480 lower deformation olivine which are both expressed in the whole scan slip-system pattern. No
 481 change is observed in the augite slip-system patterns. In the GROD angle map bands of higher
 482 internal misorientation align with regions of increased mesostasis abundance. Augite and olivine
 483 mechanical twins [white lines; {100} axis in augite (180° rotation) and olivine (60° rotation)],
 484 and regions of higher fracture density. Augite simple twins (light grey lines, 180° rotation about
 485 {001} axis) an indicator of shock deformation appear throughout both the high and lower
 486 misorientation regions. Olivine within the sample is indicated by the white transparent layer.

487



488
489
490
491
492
493

Figure 14. High strain deformation mIPF plots for augite and olivine. Nine different major slip system combinations are identified for the nakhlites that match whole section mIPF patterns. Slip-system patterns are based on the respective keys (bottom right box) where each colour indicates a different type of dominant slip-system. Olivine key: A = (010)[100], B = (010)[001], C = (100)[001], D = {0kl}[100], E = (001)[100].



494
 495 **Figure 15.** Low strain deformation mIPF plots for augite and olivine. Variation from high strain
 496 deformation slip-system patterns are observed for 9 of the 21 analysed sections. Two different
 497 low strain mIPF slip-system patterns are observed within group II, while no significant shift in
 498 pattern is observed for group V. Slip-system patterns are based on the respective keys (bottom
 499 right box) where each colour indicates a different type of dominant slip-system. Olivine key: A =
 500 (010)[100], B = (010)[001], C = (100)[001], D = {0kl}[100], E = (001)[100].

501 **4 Discussion**502 4.1 Large area electron backscatter diffraction mapping (EBSD) appropriate step-size for
503 slip-system pattern determination

504 Large area mapping for EBSD is becoming a more common tool for observing textural
505 fabrics such as CPO within samples. The ability to analyse whole thin/thick sections however, is
506 still a time-consuming and data intensive process - and is not without associated error (*e.g.*, mis-
507 indexing, improper-indexing, beam drift *etc.*) even with recent technological advancements
508 (Winiarski et al., 2021). The ability to cover larger areas is often counteracted by using larger
509 step sizes, where the limiting factor for step size is controlled by the size of the crystal (to ensure
510 >10 pixels/EBSD measurements are acquired per crystallite to adequately define its orientations),
511 sacrificing higher resolution ($\leq 4 \mu\text{m}$ step size) required for microstructural analysis (Ruggles &
512 Fullwood, 2013). Whilst microstructurally focused EBSD studies that utilise a smaller step size
513 $\leq 4 \mu\text{m}$ will often observe either multiple single crystals from specific regions of a section or a
514 selection of small areas where the total crystal count is below statistically stable results (<100 –
515 150 crystals; Vollmer, 1990; Skemer et al., 2005). Within the nakhlite datasets, five sections with
516 a step size $>4 \mu\text{m}$ (ranging from 4.5 – $15 \mu\text{m}$) were run (Table 1), where three of these sections
517 had a replicate section which was run at a step size $<4 \mu\text{m}$ (Table 1). Replicate sections for two
518 samples were also run at higher resolution (*i.e.*, step size $<4 \mu\text{m}$). Comparing these replicate
519 sections run at different step sizes clearer dominant slip-system patterns are able to be discerned
520 from $\leq 4 \mu\text{m}$ particularly with smaller area maps. However, data presented here suggests that
521 confirmation of similar slip-system patterns across multiple sections could be achieved using
522 larger step sizes $>4 \mu\text{m}$ on the condition that at least one of the sections is run at $\leq 4 \mu\text{m}$.

523 *4.1.1 Analytical limitations and essential criteria for slip-system determination in large*
524 *area EBSD datasets*

525 Comparing results between replicate datasets, little difference is observed in the GROD
526 angle distribution patterns between each section. However, the lower resolution in some of the
527 datasets makes it more difficult to accurately assess the variability in GROD angle across a given
528 crystal *i.e.*, larger GROD angles are observed where most of the crystal is at a single value (*e.g.*,
529 Fig. 8). The lower resolution of specific datasets also makes it difficult to ascertain the presence
530 and interaction between a given crystal and any mechanical twinning present (Fig. 5).
531 Comparing mIPF plots for the replicate sections, the number of crystals analysed is observed to
532 have a greater impact on the determination, refinement, and identification of the samples
533 dominant active slip-system over the specific step size of the analysis (Figs. 4, 14, and 15), with
534 the caveat that the chosen step size is appropriate for the identification of slip-systems *i.e.*, ≤ 4
535 μm . Note that this observation is only relevant when assessing the overriding major dislocation
536 slip-system expressed within a section. In order to investigate microstructural changes between
537 different regions throughout the sample, assess the higher and lower deformation regions within
538 the nakhlite samples (Figs. 5–13, Table 2), inspect secondary slip-systems contributing to a given
539 sample, or investigate how sub-crystal boundary interactions in combination with crystal
540 orientation contribute to the overall observed deformation then a higher resolution step size ≤ 4
541 μm is required.

542

4.1.2 Is large area EBSD derived slip-systems whole rock representative?

543 Analysis of the replicate sections revealed consistent augite and olivine slip system
 544 patterns for whole section, high deformation and low deformation datasets within Governador
 545 Valadares, NWA 998, and Y 000749 (Figs. 14 and 15, Table 2). However, the same correlation
 546 is not observed within the replicate Nakhla or Y 000593 sections (Figs. 14 and 15, Table 2). For
 547 the two Nakhla replicate sections there is consistency in the slip-system patterns of augite for all
 548 three datasets (whole section high deformation, and low deformation) and a discrepancy in
 549 expression of slip-system patterns in olivine where the types of slips are present in both but the
 550 dominantly expressed slip-system is different for whole section and high deformation datasets.
 551 The difference in expressed olivine slip-system patterns could be a function of the crystal
 552 differential (40 crystals and 26,340 datapoints) between the two datasets, the modal distribution
 553 of crystals between the sections, the larger (15 μm) step size of section WAM 12965 compared
 554 to USNM 426-1 (3 μm ; Table 1), or the heterogeneous influence and distribution of shock
 555 between the two sections in relation to olivine's location. More consistent MUD patterns are
 556 observed for augite within section USNM 426-1 (MUD = 0.53–1.37) compared to section WAM
 557 12965 (MUD = 0.35–2.48) despite both datasets containing statistically relevant amounts of
 558 crystals, unlike the olivine mIPF plots (Fig. 13). A similar fluctuation in MUD values is also
 559 observed between the two replicate Governador Valadares sections. In this instance, consistent
 560 slip-system patterns for all three datasets are observed, where each of the large area EBSD maps
 561 sample equivalent areas olivine (9 crystals each) and augite crystals (93 vs. 137 crystals; Fig. 4,
 562 Table 2). The only difference being a similar analysis step size discrepancy between the two
 563 Governador Valadares replicate sections as Nakhla (Table 1). For both NWA 998 replicate
 564 sections which have a 0.5 μm step size differential and Y 000749 replicate sections which have
 565 the same analysis step size no fluctuations are observed in the dominant augite and olivine slip-
 566 system patterns Across the nakhlite datasets statistically relevant crystal sets at $<4 \mu\text{m}$ step size
 567 were observed to have cleaner MUD distribution patterns and narrower MUD ranges [*e.g.*,
 568 Governador Valadares MUD = 0.35–4.55 vs 0.25–3.56 (augite mIPF) and MUD = 0.55–2.72 vs.
 569 0.35–2.68 (olivine mPF) for sections BM.1975,M16,P8469 and BM.1975,M16,P19783,
 570 respectively; Fig. 4, 14 and 15, Table 1]. Where decreased crystal count and larger step sizes
 571 contribute to increased MUD distributions within the mIPF plots [*e.g.*, Nakhla MUD = 0.63–2.30
 572 vs 0.27–5.26 (augite mIPF) and 0.53–1.37 vs. 0.34–2.48 (olivine mIPF) for sections USNM 426-
 573 1 and WAM 12965, respectively; Figs. 4, 14, and 15; Table 2]. Suggesting that differences
 574 observed within Nakhla's replicate section olivine slip-system patterns is most likely to be the
 575 result of both analysis step size and analysis area.

576 Out of all the replicate sections, only the Y 000593 sections exhibited completely
 577 different augite mIPF slip-system patterns {(100)[001]:(001)[100] and multiple slip-systems for
 578 sections 106-A and 127-A, respectively} and olivine mIPF slip-system patterns {(010)[001] with
 579 {hk0}[001] and (010)[100]+(010)[001] for sections 106-A and 127-A, respectively} which in a
 580 low strain mantle system would indicate low temperature moderate strain conditions for section
 581 106-A and high temperature low strain condition for section 127-A (Figs 12–15). Even when
 582 assessing the low deformation regions only the slip-system patterns for both olivine and augite
 583 express wildly different extrinsic parameter conditions (Fig. 12, Table 2). mIPF patterns for
 584 section 127-A indicate multiple slip-systems and augite and olivine (010)[100]+(010)[001] slip-
 585 systems which cluster towards (010)[100] slip (Fig. 12). The combination of slip-system patterns
 586 within both augite and olivine suggests deformation within section 127-A to have occurred under

587 high temperature conditions (Figs. 14 and 15). Multiple slip-systems observed within the augite
588 mIPF have been associated with partial melting and recrystallisation conditions (Fig. 15; Ave
589 Lallemand, 1978). Suggested higher temperature conditions from mIPF slip-system patterns
590 would be consistent with observed olivine annealing textures [120° triple junctions in clustered
591 olivine within Y 000593 (127-A); Fig 12] and lower dispersed deformation (GROD angle
592 values), which are not observed within Y 000593 (106-A). For section 106-A clear banding of
593 high deformation can be observed within the GROD angle map, where slip-system patterns even
594 within the low deformation regions still express high deformation region signatures (Table 2).
595 Deformation, particularly that associated with shock metamorphism, is known to be
596 heterogeneous (Stöffler et al., 2018). Variability in temperature and pressure resulting from
597 hypervelocity impacts can create pockets within a sample that may have experienced higher
598 temperature and/or pressure conditions. Furthermore, recrystallisation has been shown to
599 override a given crystal's deformation history to its new recrystallised conditions (Muto et al.,
600 2011; Wenk & Tomé, 1999; Yao et al., 2019). Annealing on the other hand has been shown to
601 significantly reduce, overprint, and sometimes completely override a given crystal's former
602 deformation history to the current conditions acting on the sample during the annealing process
603 (Farla et al., 2011; H. Jung et al., 2006). Investigations of shock deformation within the Yamato
604 nakhlites has shown some of the lowest bulk shock pressures (5–14 GPa for Y 000593) within
605 the already low shocked nakhlites (Fritz, Artemieva, et al., 2005). However, the presence of
606 annealing within the sample could have contributed to the lower inferred shock pressure values.
607 Thus, the differences in slip-system patterns observed between the two Y 000593 sections could
608 therefore indicate either an extreme change in emplacement environment, which would have had
609 to occur within the mm scale of the meteorite stone (Imae et al., 2005), shock banding within the
610 meteorite, or could indicate that the two sections represent two distinct neighbouring geological
611 units present within the same meteorite stone.

612 *4.1.3 Large area EBSD derived slip-systems for extrinsic parameter determination*

613 Studies on assessing crystallographic slip-systems at a statistically relevant scale are still
614 in their infancy. This is predominantly due to the specific cost, time, and equipment constraints
615 (*e.g.*, beam stability, indexing time, computer processing ability, post processing time *etc.*)
616 required to run ≤ 4 μm step size large area EBSD experiments. Comparison between collected
617 EBSD datasets show that in order to use crystallographic slip-systems to assess extrinsic
618 parameters within a given sample, higher resolution (step sizes ≤ 4 μm) large area EBSD is
619 required to ensure reasonable and rational results (Figs. 4, 14, and 15). Rocks in general are not
620 homogeneous, while rocks that have experienced shock metamorphism (which in the case of
621 MIL 03346, Lafayette, and most likely the entire nakhlite suite occurred on at least two
622 occasions; Daly et al., 2019) exhibit even higher levels of microstructural and mineralogical
623 heterogeneity (*e.g.*, Figs. 5–13), through increased fracturing, partial melting, and partial
624 recrystallisation (Stöffler et al., 2018). Experimental data has shown that a crystal's orientation
625 relative to external deformation parameters is one of many important factors for the selection and
626 activation of particular slip-systems (Bascou et al., 2002; Bernard et al., 2019; Kollé & Blacic,
627 1982; Müller et al., 2008). Therefore, a relationship between CPO formation and slip-system
628 activation would be expected even if it is not direct (Bascou et al., 2009; Karato et al., 2008;
629 Katayama et al., 2005; Müller et al., 2008; Nagaya et al., 2014). The presence of CPO within a
630 sample for post emplacement deformation, such as shock metamorphism, should therefore help
631 contribute to the development of a dominant slip-system being activated within a given sample

632 through increasing the number of crystals oriented in a similar geometry with respect to the
633 external strain field (Müller et al., 2008; Satsukawa & Michibayashi, 2009). Rocks, such as the
634 nakhlites and other types of meteorites, which lack majority of the geological context used for
635 terrestrial crystallographic deformation studies, such as sample orientation, require these larger
636 datasets to begin to enable valid interpretations to be made from the data. We would even go so
637 far as to insist that for samples such as meteorites slip-systems from multiple phases should be
638 considered (where possible) to help counteract the lack of geological context and often the
639 smaller amount of available sample for analysis before crystallographic slip-systems are used to
640 infer extrinsic deformation parameters for a sample as opposed to a singular crystal.

641 4.2 The correlation between slip-system signature and deformation conditions observed 642 in the nakhlites

643 In order to compare observed slip-systems in both olivine and augite (Figs. 14 and 15,
644 Table 2) to deformation parameters, existing olivine diagrams (Fig. 16) have been modified and
645 equivalent diagrams created for clinopyroxene (Fig. 17) using data from the literature. Note that
646 the current extrinsic parameters presented in Figures 16 and 17 are based on low strain (*i.e.*,
647 mantle induced) observations and experiments not naturally occurring specimens exposed to
648 high strain rates such as the nakhlites. Studies assessing mantle olivine have shown that extrinsic
649 parameters for slip-systems can be much lower in value for natural occurring samples compared
650 to laboratory studies (Bernard et al., 2019) and references therein. It is therefore possible that the
651 exact extrinsic parameters (axis values) stated for mantle augite and olivine in Figures 16 and 17
652 will be subject to change and may not be directly comparable to the presented data. However, the
653 positioning of each slip-system signature relative to one other will remain constant enabling the
654 use of both Figure 16 and 17 in a more qualitative manner.

655 Comparison of slip-system signatures in laboratory studies for both clinopyroxene and
656 olivine has shown that although there are preferred slip-systems activated along crystallographic
657 planes under specific certain conditions within a given mineral (Avé Lallemant, 1978; Bystricky
658 & Mackwell, 2001; Gueguen & Nicolas, 1980; Ingrin et al., 1991; Jaoul & Raterron, 1994; Kollé
659 & Blacic, 1982; Zhang et al., 2006), a given slip plane is not necessarily tied to any specific set
660 of universal extrinsic parameters. These identified extrinsic parameters are also not specifically
661 transferrable to different minerals, even those that share the same crystal symmetry due to the
662 contribution of intrinsic parameters. Thus, even if naturally occurring sample data were available
663 to construct Figure 17 there would still be overlap in slip-system regions between Figures 16 and
664 17, where CPO has been activated in one mineral and not another. These regions of slip-system
665 overlap could potentially lend towards the use of multiple mineral slip-systems to better refine
666 deformation parameters, if the extrinsic parameter values were properly quantified for the sample
667 (unlike the nakhlites presented here). Note that for Figure 17 there is currently not enough
668 existing data regarding the effect of water content on clinopyroxene slip-system signatures to
669 realistically discuss this intrinsic parameter for the here presented nakhlites. Thus, the presented
670 results will only be discussed in terms of the external parameters: temperature and strain.

671 Variation between identified high and low deformation regions within the nakhlites
672 identified from GROD angle maps suggest localisation of deformation within the nakhlites (*e.g.*,
673 Fig. 5). The identification and localisation of mechanical twinning within identified high
674 deformation regions suggest that the high deformation bands are related to shock deformation.

675 This interpretation is in line with observed mIPF slip-system patterns (discussed below) and
 676 previous analysis of the nakhlites where shock levels were calculated to range between 5-20 GPa
 677 (Fritz, Artemieva, et al., 2005).

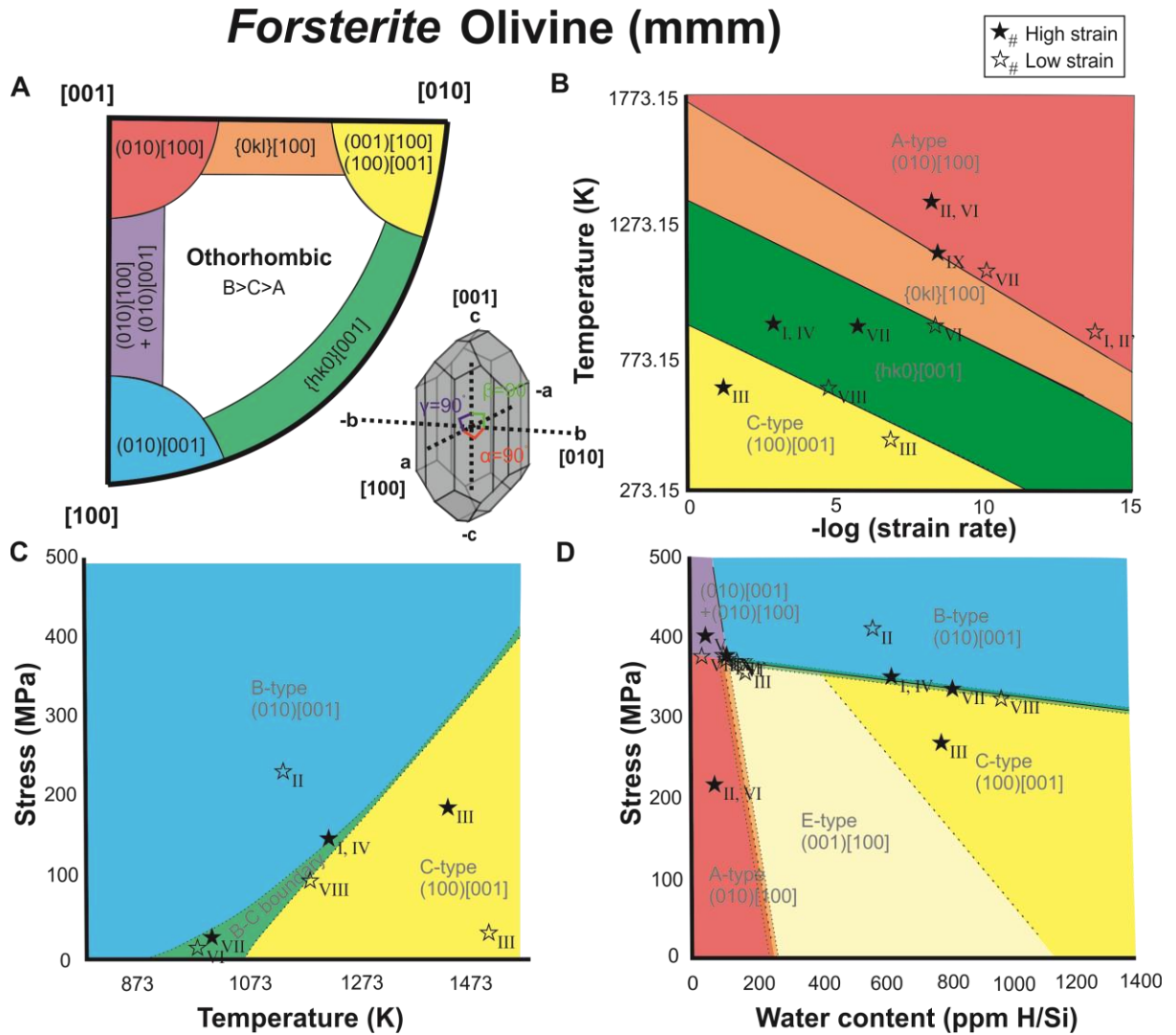
678 *4.2.1 Impact deformation regime from mIPF slip-system patterns*

679 Similarities between whole section and high deformation region compared to low
 680 deformation region mIPF slip-system patterns suggest that the localised high deformation
 681 regions are more prevalent in the nakhlites than the low deformation region deformation source.
 682 Out of the nine identified groups five express slip-system patterns more related to low
 683 temperatures and high strain, while the other three (Groups V–VII, and IX) appear to be more
 684 dominated by higher temperature deformation Figs 14, 16, and 17).

685 Within the mineral olivine the direction of slip along the {010} lattice plane tends to
 686 respond the most significantly to temperature, whilst slip associated with either the {100} or
 687 {001} lattice plane appear to respond more readily to changes in strain (Fig. 16). For the
 688 nakhlites three of the six most commonly observed slip-system patterns are associated with
 689 strain. Comparison between whole section, high deformation, and low deformation region results
 690 show that these specific slip-systems, the most significant being {hk0}[001], is observed to
 691 increase in intensity in the high deformation regions (Figs. 4, 14, and 15; Table 2).

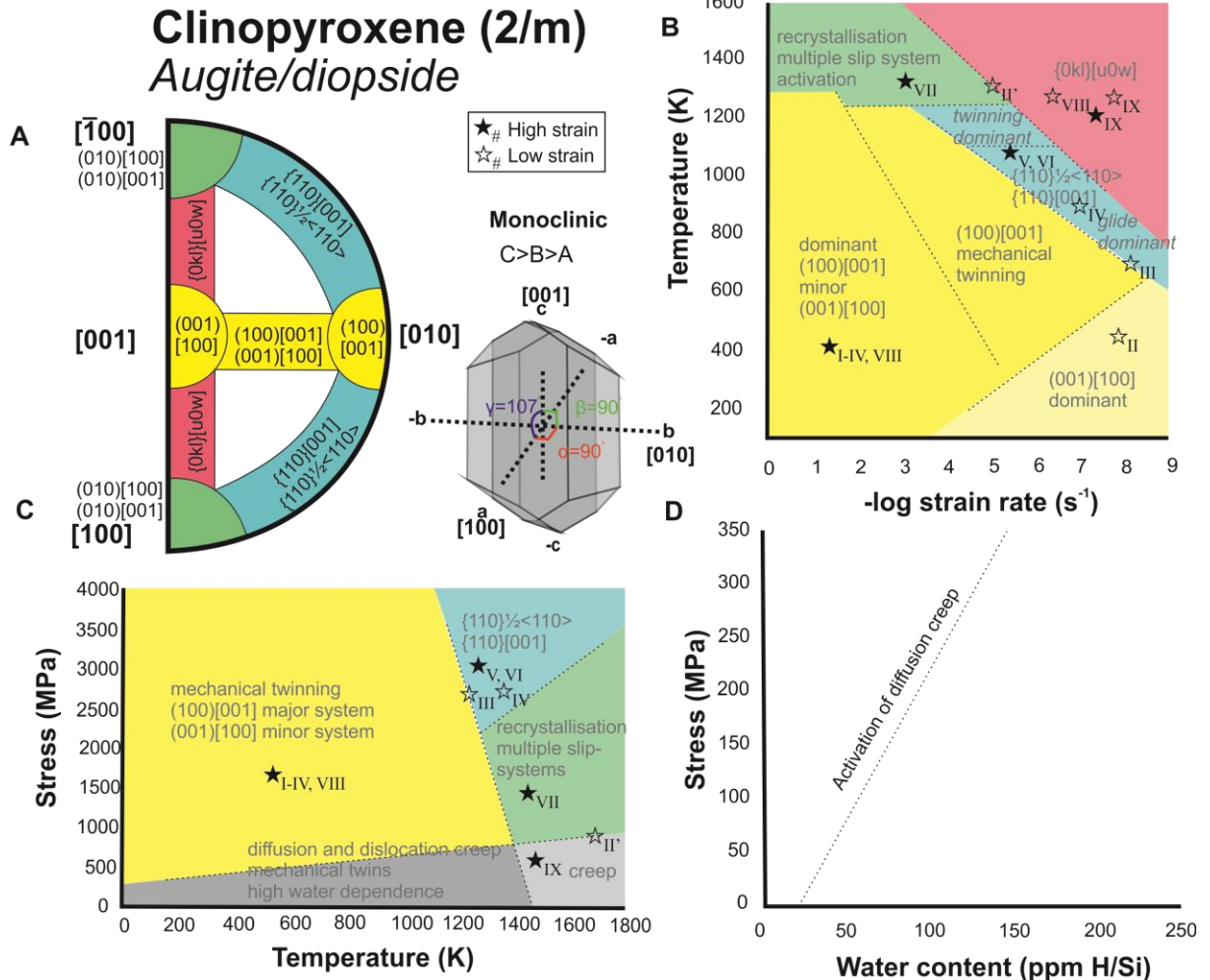
692 Augite within the nakhlites is observed to deform preferentially in the direction of <001>
 693 and <010> (Fig. 2). These preferences result in the commonly observed (100)[001] : (001)[100]
 694 slip-system patterns (Fig. 2) identified at most Earth relevant temperature, pressure, stress, and
 695 strain conditions (Fig. 17). This preferential occurrence in (100)[001] : (001)[100] slip-system
 696 mIPF pattern matches observed crystallographic preferred orientation (CPO) patterns from
 697 naturally occurring samples, where high levels of compression for <010> and perpendicular
 698 alignment to the principal strain axis for <001> is observed (Frets et al., 2012; Mauler et al.,
 699 2000). Experimental studies have shown the amount of (001)[100] slip present in a given sample
 700 is observed to increase in response to greater amounts of strain at low temperatures (Fig. 17).
 701 Between whole and high section mIPF results a slight increase in (001)[100] is observed within
 702 some of the samples (*e.g.*, Fig. 12). Both groups I and II, encompassing eight of the 16 analysed
 703 stones, exhibit mIPF patterns that relate increased proportions of (001)[100] slip within the
 704 (100)[001] : (001)[100] pairing (Fig 14). When comparing between the high deformation and
 705 low deformation regions, for all nakhlites exhibiting augite (100)[001]:(001)[100] mIPF slip-
 706 system patterns, the intensity of (001)[100] is observed to decrease in the low deformation mIPF
 707 plots (Fig. 15; Table 2). This indicates an increase in low temperature high strain deformation
 708 being present within high deformation regions within the nakhlites.

709 Assessment of mIPF slip-system patterns suggest that impact deformation within the
 710 nakhlites is typically expressed as {hk0}[001] slip in olivine and increased proportions of
 711 (001)[100] within the (100)[001] : (001)[100] slip system pairing in augite (Figs 14 and 15).
 712 However, it should be noted that the expression of impact induced deformation is not solely
 713 restricted to the high GROD angle regions within a given nakhlite sample. Many of the low
 714 deformation region mIPF slip-system patterns observed within the nakhlites still express
 715 remnants of the low temperature, high strain slip (Fig. 15, Table 2).



716
717
718
719
720
721
722
723
724

Figure 16. Known olivine (forsterite) slip-system deformation regions key (unit cells $B > C > A$). Colours indicate different slip-system regions. A) orthorhombic fundamental region slip-system key modified from (Ruzicka & Hugo, 2018) with a sketch of an olivine crystal illustrating its orthorhombic symmetry. B) Temperature vs. strain rate modified from (Katayama et al., 2004). C) Stress vs. Temperature modified from (Karato et al., 2008). D) Stress vs water content modified from (Karato et al., 2008). Note extrinsic parameters are based off low strain data. Note the placement of the identified nakhlite groupings (stars; Table 2) is only an indication of the related region and not absolute values.



725
 726 **Figure 17.** Proposed deformation conditions for clinopyroxene (augite/diopside) slip-systems
 727 key (unit cell C>B>A) based on experimental data. Colours indicate different slip-system
 728 regions. A) monoclinic fundamental region slip-system key for unit cell C>B>A with a sketch of
 729 an augite crystal illustrating its monoclinic symmetry. B) Temperature vs. strain rate (Ave
 730 Lallemand, 1978; Kollé & Blacic, 1982; Raleigh, 1967). C) Stress vs. Temperature (Ave
 731 Lallemand, 1978; Bystricky & Mackwell, 2001; Jaoul & Raterron, 1994; Kollé & Blacic, 1982;
 732 Müller et al., 2008; Zhang et al., 2006; Zhang & Green, 2007). D) Stress vs water content (Hier-
 733 Majumder et al., 2005). Due to the paucity of experimental data involving augite deformation in
 734 the presence of water, currently we can only state that there is a trend of lower extrinsic
 735 parameters required to induce the activation of specific slip-system signatures in augite with
 736 increased water content. Note extrinsic parameters are derived from low strain data. Note the
 737 placement of the identified nakhlite groupings (stars; Table 2) is only an indication of the related
 738 region and not absolute values.

739 **4.2.2. Emplacement, low finite strain from mIPF slip-system pattern signatures**

740 The occurrence of high deformation bands within the nakhlites in conjunction with their
 741 observed slip-system mIPF patterns indicating deformation related impact, suggests that the low
 742 deformation regions may provide evidence for emplacement deformation. Out of the 16 analysed

743 nakhlites, only four stones showed evidence for high temperature deformation within the high
 744 deformation regions [Y 000749 (group V), MIL 090030 (group VI), MIL 090136 (Group VII),
 745 and Y 000593 (127-A; group IX); Figs 9–11, and 13, respectively]. The high temperature slip-
 746 system patterns observed in these regions were only seen to intensify in MUD values within the
 747 low deformation regions mIPF plots (Figs. 14, 15). For augite slip in these groups is observed to
 748 occur along the {110} lattice or along multiple slip planes (Fig. 2, 15, and 17) and for olivine slip
 749 is predominantly observed to incorporate (010)[100] (Fig. 1, 14, and 16). It should be noted that
 750 the samples attributed to groups V–VII, and IX all exhibited low detected GROD angles within
 751 the map areas (Figs. 9–11, and 13). For identified groups I–IV, and VIII which all exhibit impact
 752 related slip-system patterns had at least one analysed section within the group that exhibited
 753 identifiable shifts in mIPF slip-system patterns between high and low deformation regions (Table
 754 2). Assessment of the low deformation regions express mIPF slip-system patterns for those
 755 sections show shifts that emphasise patterns related to (010)[001] or (001)[100]/(100)[001] in
 756 olivine and (100)[001] in augite (Fig 15). (010)[100] slip is a common slip-system observed in
 757 mantle olivine's on Earth (Fig. 16; (Bernard et al., 2019; Girard et al., 2013; Ohuchi et al., 2011;
 758 Yao et al., 2019). The presence of (100)[001] slip in augite is also commonly observed within
 759 nearly all naturally forming Earth samples (Bascou et al., 2002; Godard & van Roermund, 1995).
 760 Ultimately the slip-system patterns observed within these samples are typically associated with
 761 relatively low-moderate temperatures and low strain conditions (Figs. 16 and 17) indicating that
 762 they are indeed remnants of emplacement deformation within the nakhlites that have been
 763 subsequently overprinted by shock deformation.

764 4.2.2. Dominant clinopyroxene slip-systems

765 From the two analysed minerals augite shows the least diversity in mIPF slip-system
 766 patterns (Table 2). Laboratory experiments have shown that clinopyroxene slip-systems are
 767 strongly influenced by crystal orientation relative to the principal strain axis for the activation of
 768 specific slip-systems (Avé Lallemand, 1978; Bascou et al., 2002; Kollé & Blacic, 1982).
 769 Clinopyroxenes, including augite, have one of the lowest forms of crystal symmetry (monoclinic,
 770 2/m). The relationship between augite's crystallographic axes ($\alpha = 107^\circ$, $\beta = 90^\circ$, and $\gamma = 90^\circ$),
 771 where the crystallographic length of $\langle c \rangle > \langle a \rangle$, for augite's unit cell, will often require either
 772 specific orientation and/or higher strain for activation of slip-systems other than (100)[001] :
 773 (001)[100], such as {h0l} to form. Laboratory studies have also shown that even when such
 774 specific conditions are met to activate another of augite's slip-systems, (100)[001] : (001)[100]
 775 slip-systems will also often be observed within the sample (Ave Lallemand, 1978; Kollé &
 776 Blacic, 1983; Philippot & van Roermund, 1992).

777 For any geological sample, a variety of observed different slip-systems within a single
 778 sample would be expected. The expectation of variable slip-systems is in part due to the variation
 779 in alignment of crystals within a given rock and each crystal's local petrological context and
 780 surrounding mineral assemblage. For igneous samples, >50 % crystal alignment is considered as
 781 strong fabric (Bunge, 1982; Vollmer, 1990). In the nakhlites, augite exhibits S- to LS-type fabric
 782 where crystal alignment ranges from 8–26 % (Griffin et al., n.d.). The higher percentage of
 783 random crystal orientations within any given sample coupled with a high dependence on crystal
 784 orientation for the activation of slip-system signatures will naturally result in multiple slip-
 785 system development between crystals. However, just like shape preferred orientation (SPO) and
 786 CPO within a rock, in order to assess representative deformation across a given sample several

787 crystals preferentially on a similar level for statistical relevance (*i.e.*, ≥ 100 –150 crystals) would
788 need to be assessed (Skemer et al., 2005; Vollmer, 1990). Overall, despite the low crystal
789 symmetry and higher slip-system activation criteria in clinopyroxenes, differences between
790 certain extrinsic conditions, *e.g.*, low temperature and high pressure, high temperature low
791 pressure, high temperature and pressure *etc.* can be observed (Fig. 17). However, studies so far
792 indicate for most Earth relevant conditions the changes in slip-systems will be more subtle and
793 be predominantly focused on shifts within the (100)[001] : (001)[100] slip-system pairing.
794 Although clinopyroxene slip-systems have been identified to associate with specific conditions,
795 there is a lot more work to be done. In particular, more information is needed addressing natural
796 formation conditions and the effect of water content, before clinopyroxene slip-systems can be
797 definitively used with the same level of certainty as geologists currently use olivine.

798 4.3 Implications for the nakhlites' time on Mars

799 Across the 16 analysed nakhlite meteorites nine distinct mIPF slip-system pattern
800 combinations for whole section data are observed (Fig. 4) that reflect high strain deformation
801 (Fig. 14). These mIPF slip-systems, when separated into respective high and low deformation
802 regions (Figs, 14 and 15, Table 2), indicate signatures that most likely reflect differences in
803 shock deformation. Even low deformation regions within the analysed nakhlites show a strong
804 influence of high strain deformation (*e.g.*, shock) over low strain deformation signatures (*e.g.*,
805 mantle). Hence the extrinsic parameters presented in Figures 16 and 17 will not be applicable to
806 the nakhlites but the relationship between the different slip-systems can be applied. On this basis,
807 the presented data show several different high-strain deformation environments from within the
808 nakhlite source indicating heterogenous sampling of the ejection crater.

809 Comparison between whole section, high deformation, and low deformation region slip-
810 system patterns across the 21 analysed sections show an increase in the slip-system patterns of
811 {hk0}[001] in olivine and an increased (001)[100] component within the dominant augite
812 (100)[001] : (001)[100] signature in high deformation regions. These particular slip-systems
813 have been shown in mantle rocks to indicate increase strain at low temperatures (Figs. 16 and 17;
814 Cordier, 2002; Katayama et al., 2004; Kollé & Blacic, 1983; Mainprice et al., 2005; Mauler et
815 al., 2000), which suggests that this particular olivine-augite slip-system combination often
816 expresses as the dominant or secondary slip-system pattern within the identified nakhlite groups,
817 particularly groups I–IV and VIII (Figs. 5–9, 12–14, Table 2), could be indicative of shock-
818 induced deformation. However, further investigations involving high strain experiments
819 simulating hypervelocity impacts for both olivine and augite would be required to confirm if
820 these slip-systems are preferentially activated during shock deformation processes or if they are
821 in fact related to other low strain factors within the nakhlite source environment.

822 The establishment of olivine slip-systems under low-strain extrinsic parameters are well
823 constrained where the influences of the extrinsic parameters are an ongoing and active field of
824 research (Bernard et al., 2019). The relationship of augite to extrinsic parameters, on the other
825 hand, has not been as consistently studied olivine but has gained serious momentum over the last
826 decade [*e.g.*, Bascou et al. (2011), Tedonkenfack et al. (2021), and Van der Werf et al. (2017)].
827 Presented in this study is the first attempt to collate existing clinopyroxene slip-system data to
828 begin thinking about clinopyroxene slip-systems in a similar manner to olivine with respect to
829 extrinsic parameters. Through comparing observed clinopyroxene (in this instance augite) MIPF

830 slip-system patterns against published experimental data and the more-established olivine slip-
831 system extrinsic parameters to ascertain patterns and commonalities (due to the data pertaining to
832 low strain parameters), rough implications with respect to the nakhlites can be drawn. All of the
833 identified groups apart from groups V–VII, and IX (Figs. 9–11, and 13, respectively; Table 2)
834 exhibit slip-system patterns that are highly influenced by high strain deformation (Fig. 14, Table
835 2). Groups V–VII and IX express slip-system patterns commonly associated in mantle rocks with
836 high temperature deformation the difference being group V exhibiting patterns indicative of
837 higher strain and group IX indicating mIPF slip-system patterns potentially related to annealing
838 processes (Figs. 9, 13, 16 and 17).

839 Separation of the high and low deformation regions within the nakhlites show that
840 interpretation of mantle derived parameters is more complex than just assessing regions of low
841 deformation within the samples. Despite the nakhlites being described as low shock samples [5–
842 20 GPa (Fritz, Artemieva, et al., 2005; Fritz, Greshake, et al., 2005)], mIPF slip-system patterns
843 even within the low deformation regions still exhibit weakened high deformation region
844 signatures, most likely formed as the result of shock deformation (Fig. 15). This finding could
845 support the hypothesis of the nakhlite ejecta crater being positioned on the extremity of an older
846 crater (Daly et al., 2019). Out of all the analysed samples only 9 of the 21 sections showed
847 significant shifts in either olivine and/or augite major mIPF slip-system patterns between
848 separated high and low deformation regions (Table 2, Figs. 14 and 15). In these particular
849 samples, an increase in the MUD is observed within less dominant mIPF slip-systems patterns
850 and a weakening of the MUD for olivine {hk0}[001] and augite (001)[100] is typically observed.
851 The implications of these observations indicate that there is potential for the minor slip-systems
852 observed to increase in MUD intensity within the mIPF low deformation region plots could
853 indicate nakhlite mantle related deformation. However, further investigation is required before
854 any interpretations could be made.

855 The current groupings presented in Figures 4, 14, 15, and Table 2 indicate samples that
856 share similar extrinsic parameters related to high strain deformation. This could be interpreted as
857 samples exposed to similar conditions within the ejecta crater during launch. These groupings do
858 not indicate that the samples are sourced from the same magmatic body as is evidence by
859 samples MIL 03346 and NWA 817 within identified group II that show different slip-system
860 patterns within their low deformation region mIPF plots despite sharing the same whole section
861 and high deformation slip-system signatures (Table 2, Figs. 14 and 15). The same observation
862 can be applied to the proposed ‘paired’ Yamato and Miller Range nakhlites were different mIPF
863 slip-system patterns are observed for both whole section (Fig. 4) and identified low and high
864 deformation regions (Figs. 14 and 15, Table 2).

865 For the Yamato nakhlites, here categorised into groups I, V, VIII, and IX (Figs. 9, 12, and
866 13, Table 2) mIPF slip-system patterns express temperature differences that could not be
867 resolved if they were located in the same position within the nakhlite ejecta crater and formed
868 from the same magma body on Mars (Figs. 16 and 17). For the Miller Range nakhlites samples
869 such as MIL 03346 and MIL 090032 could be related based off observed slip-system patterns
870 (Figs. 6, 14, and 15, Table 2). However, both MIL 090030 (Fig. 10) and MIL 090030 (Fig. 11)
871 exhibit mIPF slip-system patterns whose extrinsic parameters do not support pairing with any of
872 the Miller Range nakhlites (Figs. 4, 14, and 15, Table 2).

873 Apart from the two Y 000593 sections, discussed above, each of the different Miller
874 Range and Yamato samples are sourced from separate stones that were found in a similar
875 location in Antarctica (Treiman, 2005). These locations are known glacial fields that are fed from
876 a large catchment area. The variation observed in mIPF slip-system patterns between these
877 ‘paired’ stones implies different deformation parameters for the separate meteorites, which could
878 indicate either a range of deformation environments with each meteorite being sourced from a
879 different section within the same igneous body or could suggest that each individual meteorite
880 represents its own separate flow/intrusion. From rudimentary modelling of the nakhlite
881 emplacement parameters, magma body unit thicknesses greater than ten meters were suggested
882 for the Miller Range nakhlites, while the Yamato nakhlites were suggested to have magma body
883 unit thicknesses less than ten meters (Griffin et al., n.d.). The smaller modelled unit thicknesses
884 in conjunction with the observed differences in crystallographic deformation, similar recovery
885 position, and geochronological dating (Cohen et al., 2017), currently supports the hypothesis that
886 the Yamato individual nakhlites formed as individual igneous units that were located in close
887 proximity to one another on Mars while the larger unit thicknesses, current geochronological
888 dating in combination with presented crystallographic slip-systems would suggest that the Miller
889 Range nakhlites could represent different regions (or lobes) from a single igneous event (Griffin
890 et al., n.d.). Overall, variation in slip-system patterns observed from presented data, suggests that
891 the suite of nakhlites meteorites heterogeneously sample different areas from within their launch
892 crater on Mars, sampling a variety of different igneous units.

893 **5 Conclusions**

894 Observed slip-system patterns can be used to discern between samples exposed to
895 varying extrinsic parameters. However, more work (both natural samples and laboratory based)
896 needs to be undertaken to further constrain slip-system signature extrinsic parameters,
897 particularly regarding the effects of high strain and water content. In addition, large area EBSD
898 has the potential to become a powerful technique to constrain extrinsic parameters associated
899 with deformation (*i.e.*, pressure, temperature, strain, water content) of Martian magmas and other
900 meteorites when combined with analysis of naturally occurring samples and laboratory
901 experiments regarding slip-system activations.

902 Combined olivine and clinopyroxene mIPF slip-system patterns identified nine different slip-
903 system pattern combinations within the nakhlites five of which were associated with high strain
904 deformation interpreted as shock deformation. This shock (high strain) deformation is observed
905 as increased proportions of (001)[100] in augite and {hk0}[001] in olivine. Investigation of slip-
906 system patterns between identified high and low deformation regions within the data indicate
907 high strain deformation to be prevalent through the sample, including within the low deformation
908 regions. Less dominant slip-system patterns identified to increase in MUD intensity within the
909 low deformation slip-system patterns could have the potential to represent low strain (mantle
910 related) deformation. However, further work investigating the contributions of shock
911 metamorphism and the exact relationship between high strain slip-system extrinsic parameters is
912 required.

913 **Acknowledgments, Samples, and Data**

914 For providing the samples used in this study we thank the NHM London, Japanese Antarctic
 915 Meteorite Research Centre, Smithsonian, NASA Meteorite Working Group, Macovich
 916 Collection, The Museum of Western Australia, Centre Européen de Recherche et d'Enseignement
 917 de Géosciences de l'Environnement (CEREGE), and the Institute of Meteoritics University of New
 918 Mexico. This work was funded by the Science and Technology Facilities Council through grants
 919 ST/N000846/1 and ST/H002960/1 to M.R.L). All data are available at
 920 DOI:10.5281/zenodo.5545821.

921 **References**

- 922 Ashby, M. F. (1970). The deformation of plastically non-homogeneous materials. *Philosophical Magazine*, *21*(170),
 923 399–424. <https://doi.org/10.1080/14786437008238426>
- 924 Ashby, M. F. (1983). *Mechanisms of Deformation and Fracture. Advances in Applied Mechanics* (Vol. 23).
- 925 Avé Lallemant, H. G. (1978). Experimental deformation of diopside and websterite. *Tectonophysics*, *48*(1–2), 1–27.
 926 [https://doi.org/10.1016/0040-1951\(78\)90083-5](https://doi.org/10.1016/0040-1951(78)90083-5)
- 927 Avé Lallemant, H. G. A. (1978). Experimental deformation of diopside and websterite. *Tectonophysics*, *48*, 1–27.
- 928 Barber, D. J., Wenk, H. R., Hirth, G., & Kohlstedt, D. L. (2010). *Chapter 95 Dislocations in Minerals. Dislocations*
 929 *in Solids* (Vol. 16). Elsevier. [https://doi.org/10.1016/S1572-4859\(09\)01604-0](https://doi.org/10.1016/S1572-4859(09)01604-0)
- 930 Bascou, J., Tommasi, A., & Mainprice, D. (2002). Plastic deformation and development of clinopyroxene lattice
 931 preferred orientations in eclogites. *Journal of Structural Geology*, *24*, 1357–1368.
- 932 Bascou, J., Tommasi, A., & Mainprice, D. (2009). Plastic deformation and development of clinopyroxene lattice
 933 preferred orientations in eclogites. *Journal of Structural Geology*, *24*(2002), 43603.
- 934 Bascou, J., Doucet, L. S., Saumet, S., Ionov, D. A., Ashchepkov, I. V., & Golovin, A. V. (2011). Seismic velocities,
 935 anisotropy and deformation in Siberian cratonic mantle: EBSD data on xenoliths from the Udachnaya
 936 kimberlite. *Earth and Planetary Science Letters*, *304*(1–2), 71–84. <https://doi.org/10.1016/j.epsl.2011.01.016>
- 937 Bernard, R. E., Behr, W. M., Becker, T. W., Young, D. J., & Young, David, J. (2019). Relationships Between
 938 Olivine CPO and Deformation Parameters in Naturally Deformed Rocks and Implications for Mantle Seismic
 939 Anisotropy. *Geochemistry, Geophysics, Geosystems*, *20*(7), 3469–3494.
 940 <https://doi.org/10.1029/2019GC008289>
- 941 Boneh, Y., & Skemer, P. (2014). The effect of deformation history on the evolution of olivine CPO. *Earth and*
 942 *Planetary Science Letters*, *406*, 213–222. <https://doi.org/10.1016/j.epsl.2014.09.018>
- 943 Bunch, T. E., & Reid, A. M. (1975). The Nakhilites. Part I: Petrography and mineral chemistry. *Meteoritics*, *10*, 303–
 944 315.
- 945 Bunge, H.-J. (1982). *Texture analysis in materials science: Mathematical methods*. (H.-J. Bunge, Ed.) (Paperback).
 946 Cuvillier Verlag, Göttingen. <https://doi.org/10.7312/chi-18840-001>
- 947 Bystricky, M., & Mackwell, S. (2001). Creep of dry clinopyroxene aggregates with deformation in the dislocation
 948 creep. *Journal of Geophysical Research*, *106*, 13443–13454.
- 949 Cohen, B. E., Mark, D. F., Cassata, W. S., Lee, M. R., Tomkinson, T., Smith, C. L., et al. (2017). Taking the pulse
 950 of Mars via dating of a plume-fed volcano. *Nature Communications*, *8*(1), 640.
 951 <https://doi.org/10.1038/s41467-017-00513-8>
- 952 Cordier, P. (2002). Dislocations and slip systems of mantle minerals. *Reviews in Mineralogy and Geochemistry*, *51*.
 953 <https://doi.org/10.2138/gsrmg.51.1.137>
- 954 Corrigan, C. M., Velbel, M. A., & Vicenzi, E. P. (2015). Modal abundances of pyroxene, olivine, and mesostasis in
 955 nakhilites: Heterogeneity, variation, and implications for nakhilite emplacement. *Meteoritics and Planetary*
 956 *Science*, *50*(9), 1497–1511. <https://doi.org/10.1111/maps.12492>
- 957 Daly, L., Lee, M. R., Piazzolo, S., Griffin, S., Bazargan, M., Campanale, F., et al. (2019). Boom Boom Pow: shock-
 958 facilitated aqueous alteration and evidence for two shock events in the Martian nakhilite meteorites. *Science*
 959 *Advances*, *5*(9), 1-11/eaaw5549. <https://doi.org/DOI:10.1126/sciadv.aaw5549>
- 960 Day, J. M. D., Tait, K. T., Udry, A., Moynier, F., Liu, Y., & Neal, C. R. (2018). Martian magmatism from plume
 961 metasomatized mantle. *Nature Communications*, *9*(1), 4799. <https://doi.org/10.1038/s41467-018-07191-0>
- 962 Farla, R. J. M., Kokkonen, H., Gerald, J. D. F., Barnhoorn, A., Faul, U. H., & Jackson, I. (2011). Dislocation
 963 recovery in fine-grained polycrystalline olivine. *Physics and Chemistry of Minerals*, *38*(5), 363–377.

- 964 <https://doi.org/10.1007/s00269-010-0410-3>
- 965 Fei, H., Hegoda, C., Yamazaki, D., Wiedenbeck, M., Yurimoto, H., Shcheka, S., & Katsura, T. (2012). High silicon
966 self-diffusion coefficient in dry forsterite. *Earth and Planetary Science Letters*, 345–348, 95–103.
967 <https://doi.org/10.1016/j.epsl.2012.06.044>
- 968 Fleck, N. A., Muller, G. M., Ashby, M. F., & Hutchinson, J. W. (1994). Strain gradient plasticity :theory and
969 experiment, *Acta Metal Material*, 42(2), 475–487.
- 970 Frets, E., Tommasi, A., Garrido, C. J., Padrón-Navarta, J. A., Amri, I., & Targuisti, K. (2012). Deformation
971 processes and rheology of pyroxenites under lithospheric mantle conditions. *Journal of Structural Geology*,
972 39, 138–157. <https://doi.org/10.1016/j.jsg.2012.02.019>
- 973 Friedrich, J. M., Ruzicka, A., Macke, R. J., Thostenson, J. O., Rudolph, R. A., Rivers, M. L., & Ebel, D. S. (2017).
974 Relationships among physical properties as indicators of high temperature deformation or post-shock thermal
975 annealing in ordinary chondrites. *Geochimica et Cosmochimica Acta*, 203, 157–174.
976 <https://doi.org/10.1016/j.gca.2016.12.039>
- 977 Fritz, J., Artemieva, N. A., & Greshake, A. (2005). Ejection of Martian meteorites. *Meteoritics & Planetary Science*,
978 40(9–10), 1393–1411. <https://doi.org/10.1111/j.1945-5100.2005.tb00409.x>
- 979 Fritz, J., Greshake, A., & Stöffler, D. (2005). Micro-Raman spectroscopy of plagioclase and maskelynite in Martian
980 meteorites: Evidence of progressive shock metamorphism. *Antarctic Meteorite Research*, 18, 96–116.
- 981 Girard, J., Chen, J., Raterron, P., & Holyoke, C. W. (2013). Hydrolytic weakening of olivine at mantle pressure:
982 Evidence of [100](010) slip system softening from single-crystal deformation experiments. *Physics of the*
983 *Earth and Planetary Interiors*, 216, 12–20. <https://doi.org/10.1016/j.pepi.2012.10.009>
- 984 Godard, G., & van Roermund, H. L. M. (1995). Deformation-induced clinopyroxene fabrics from eclogites. *Journal*
985 *of Structural Geology*, 17(10), 1425–1443. [https://doi.org/10.1016/0191-8141\(95\)00038-F](https://doi.org/10.1016/0191-8141(95)00038-F)
- 986 Griffin, S., Keller, T., Daly, L., Lee, M. R., Cohen, B. E., Forman, L. V., et al. (n.d.). *Emplacement of Amazonian*
987 *nakhlite igneous rocks and implications for their source volcano on Mars*.
- 988 Groves, G. W., & Kelly, A. (1963). Independent slip systems in crystals. *Philosophical Magazine*, 8(89), 877–887.
989 <https://doi.org/10.1080/14786436308213843>
- 990 Gueguen, Y., & Nicolas, A. (1980). Deformation of mantle rocks. *Annual Review of Earth and Planetary Sciences*,
991 8, 119–144.
- 992 Hallis, L. J., & Taylor, G. J. (2011). Comparisons of the four Miller Range nakhlites, MIL 03346, 090030, 090032
993 and 090136: Textural and compositional observations of primary and secondary mineral assemblages.
994 *Meteoritics and Planetary Science*, 46(12), 1787–1803. <https://doi.org/10.1111/j.1945-5100.2011.01293.x>
- 995 Hansen, L. N., Zhao, Y. H., Zimmerman, M. E., & Kohlstedt, D. L. (2014). Protracted fabric evolution in olivine:
996 Implications for the relationship among strain, crystallographic fabric, and seismic anisotropy. *Earth and*
997 *Planetary Science Letters*, 387, 157–168. <https://doi.org/10.1016/j.epsl.2013.11.009>
- 998 Henry, H., Tilhac, R., Griffin, W. L., O'Reilly, S. Y., Satsukawa, T., Kaczmarek, M.-A., et al. (2017). Deformation
999 of mantle pyroxenites provides clues to geodynamic processes in subduction zones: Case study of the Cabo
1000 Ortegá Complex, Spain. *Earth and Planetary Science Letters*, 472, 174–185.
1001 <https://doi.org/10.1016/j.epsl.2017.05.028>
- 1002 Hier-Majumder, S., Mei, S., & Kohlstedt, D. L. (2005). Water weakening of clinopyroxenite in diffusion creep.
1003 *Journal of Geophysical Research: Solid Earth*, 110(7), 1–12. <https://doi.org/10.1029/2004JB003414>
- 1004 Hunter, R. H. (1996). Texture Development in Cumulate Rocks. *Developments in Petrology*, 15(C), 77–101.
1005 [https://doi.org/10.1016/S0167-2894\(96\)80005-4](https://doi.org/10.1016/S0167-2894(96)80005-4)
- 1006 Imae, N., Ikeda, Y., & Kojima, H. (2005). Petrology of the Yamato nakhlites. *Meteoritics and Planetary Science*,
1007 40(11), 1581–1598. <https://doi.org/10.1111/j.1945-5100.2005.tb00133.x>
- 1008 Ingrin, J., Doukhan, N., & Doukhan, J. C. (1991). High-Temperature Deformation of Diopside Single-Crystal .2.
1009 Transmission Electron-Microscopy Investigation Of The Defect Microstructures. *Journal Of Geophysical*
1010 *Research-Solid Earth And Planets*, 96(B9), 14287–14297. <https://doi.org/10.1029/91JB01233>
- 1011 Jaoul, O., & Raterron, P. (1994). High-temperature deformation of diopside crystal 3. Influences of pO₂ and SiO₂
1012 precipitation. *Journal of Geophysical Research*, 99(B5), 9423–9439. <https://doi.org/10.1029/93JB03363>
- 1013 Jung, H., Katayama, I., Jiang, Z., Hiraga, T., & Karato, S.-I. (2006). Effect of water and stress on the lattice-
1014 preferred orientation of olivine. *Tectonophysics*, 421(1–2), 1–22. <https://doi.org/10.1016/j.tecto.2006.02.011>
- 1015 Jung, Haemyeong, Mo, W., & Green, H. W. (2009). Upper mantle seismic anisotropy resulting from pressure-
1016 induced slip transition in olivine. *Nature Geoscience*, 2(1), 73–77. <https://doi.org/10.1038/ngeo389>
- 1017 Kaboli, S., Burnley, P. C., Xia, G., & Green, H. W. (2017). Pressure Dependence of Creep in Forsterite Olivine:
1018 Comparison of Measurements From the D-DIA and Griggs Apparatus. *Geophysical Research Letters*, 44(21),
1019 10,939-10,947. <https://doi.org/10.1002/2017GL075177>

- 1020 Karato, S., Jung, H., Katayama, I., & Skemer, P. (2008). Geodynamic Significance of Seismic Anisotropy of the
1021 Upper Mantle: New Insights from Laboratory Studies. *Annual Review of Earth and Planetary Sciences*, 36(1),
1022 59–95. <https://doi.org/10.1146/annurev.earth.36.031207.124120>
- 1023 Katayama, I., & Karato, S. ichiro. (2006). Effect of temperature on the B- to C-type olivine fabric transition and
1024 implication for flow pattern in subduction zones. *Physics of the Earth and Planetary Interiors*, 157(1–2), 33–
1025 45. <https://doi.org/10.1016/j.pepi.2006.03.005>
- 1026 Katayama, I., Jung, H., & Karato, S. I. (2004). New type of olivine fabric from deformation experiments at modest
1027 water content and low stress. *Geology*, 32(12), 1045–1048. <https://doi.org/10.1130/G20805.1>
- 1028 Katayama, I., Karato, S. I., & Brandon, M. (2005). Evidence of high water content in the deep upper mantle inferred
1029 from deformation microstructures. *Geology*, 33(7), 613–616. <https://doi.org/10.1130/G21332.1>
- 1030 Keppler, R. (2018). Crystallographic preferred orientations in eclogites – A review. *Journal of Structural Geology*,
1031 115(April), 284–296. <https://doi.org/10.1016/j.jsg.2018.04.003>
- 1032 Kollé, J. J., & Blacic, J. D. (1982). Deformation of single-crystal clinopyroxenes: 1. Mechanical twinning in
1033 diopside and hedenbergite. *Journal of Geophysical Research*, 87(B5), 4019–4034.
- 1034 Kollé, J. J., & Blacic, J. D. (1983). Deformation of single-crystal clinopyroxenes: 2. Dislocation- controlled flow
1035 processes in hedenbergite. *Journal of Geophysical Research*, 88(B3), 2381–2393.
1036 <https://doi.org/10.1029/JB088iB03p02381>
- 1037 Krämer Ruggiu, L., Gattacceca, J., Bevouard, B., Udry, A., Debaille, V., Rochette, P., et al. (2020). Caleta el Cobre
1038 022 martian meteorite: increasing nakhlite diversity. *Meteoritics and Planetary Science*, 25, 1–25.
1039 <https://doi.org/10.1111/maps.13534>
- 1040 Law, R. D. (1990). Crystallographic fabrics: a selective review of their applications to research in structural geology.
1041 *Deformation Mechanisms, Rheology and Tectonics. Geological Society Special Publication*, 54(54), 352–355.
1042 <https://doi.org/10.1144/GSL.SP.1990.054.01.30>
- 1043 Lee, M. R., Tomkinson, T., Hallis, L. J., & Mark, D. F. (2015). Formation of iddingsite veins in the martian crust by
1044 centripetal replacement of olivine: Evidence from the nakhlite meteorite Lafayette. *Geochimica et*
1045 *Cosmochimica Acta*, 154, 49–65. <https://doi.org/10.1016/j.gca.2015.01.022>
- 1046 Li, Z. Y., Wen, D. P., Wang, Y. F., & Liu, X. (2020). An Investigation of Dislocation in Olivine Phenocrysts from
1047 the Hawaiian Basalts. *Journal of Earth Science*, 31(6), 1183–1189. [https://doi.org/10.1007/s12583-020-1338-](https://doi.org/10.1007/s12583-020-1338-2)
1048 2
- 1049 Liu, S., Tommasi, A., Vauchez, A., & Mazzucchelli, M. (2019). Deformation, Annealing, Melt-Rock Interaction,
1050 and Seismic Properties of an Old Domain of the Equatorial Atlantic Lithospheric Mantle. *Tectonics*, 38(4),
1051 1164–1188. <https://doi.org/10.1029/2018TC005373>
- 1052 Mainprice, D., Tommasi, A., Couvy, H., Cordier, P., & Frost, D. J. (2005). Pressure sensitivity of olivine slip
1053 systems and seismic anisotropy of Earth’s upper mantle. *Nature*, 433(7027), 731–733.
1054 <https://doi.org/10.1038/nature03266>
- 1055 Mainprice, D., Bachmann, F., Hielscher, R., & Schaeben, H. (2015). Descriptive tools for the analysis of texture
1056 projects with large datasets using MTEX: Strength, symmetry and components. *Geological Society Special*
1057 *Publication*, 409(1), 251–271. <https://doi.org/10.1144/SP409.8>
- 1058 Mauler, A., Bystricky, M., Kunze, K., & Mackwell, S. (2000). Microstructures and lattice preferred orientations in
1059 experimentally deformed clinopyroxene aggregates. *Journal of Structural Geology*, 22, 1633–1648.
1060 [https://doi.org/10.1016/S0191-8141\(00\)00073-0](https://doi.org/10.1016/S0191-8141(00)00073-0)
- 1061 Mei, S., & Kohlstedt, D. L. (2000). Influence of water on plastic deformation of olivine aggregates 2. Dislocation
1062 creep regime. *Journal of Geophysical Research: Solid Earth*, 105(B9), 21471–21481.
1063 <https://doi.org/10.1029/2000jb900180>
- 1064 Müller, W. F., Walte, N., & Miyajima, N. (2008). Experimental deformation of ordered natural omphacite: a study
1065 by transmission electron microscopy. *European Journal of Mineralogy*, 20, 835–844.
1066 <https://doi.org/10.1127/0935-1221/2008/0020-1851>
- 1067 Muto, J., Hirth, G., Heilbronner, R., & Tullis, J. (2011). Plastic anisotropy and fabric evolution in sheared and
1068 recrystallized quartz single crystals. *Journal of Geophysical Research: Solid Earth*, 116(2), 1–18.
1069 <https://doi.org/10.1029/2010JB007891>
- 1070 Nagaya, T., Wallis, S. R., Kobayashi, H., Michibayashi, K., Mizukami, T., Seto, Y., et al. (2014). Dehydration
1071 breakdown of antigorite and the formation of B-type olivine CPO. *Earth and Planetary Science Letters*, 387,
1072 67–76. <https://doi.org/10.1016/j.epsl.2013.11.025>
- 1073 Noguchi, T., Nakamura, T., Misawa, K., Imae, N., Aoki, T., & Toh, S. (2009). Laihunite and jarosite in the Yamato
1074 00 nakhlites: Alteration products on Mars? *Journal of Geophysical Research: Planets*, 114(10), 1–13.
1075 <https://doi.org/10.1029/2009JE003364>

- 1076 Ohuchi, T., Kawazoe, T., Nishihara, Y., Nishiyama, N., & Irifune, T. (2011). High pressure and temperature fabric
 1077 transitions in olivine and variations in upper mantle seismic anisotropy. *Earth and Planetary Science Letters*,
 1078 304(1–2), 55–63. <https://doi.org/10.1016/j.epsl.2011.01.015>
- 1079 Philippot, P., & van Roermund, H. L. M. (1992). Deformation processes in eclogitic rocks: evidence for the
 1080 rheological delamination of the oceanic crust in deeper levels of subduction zones. *Journal of Structural*
 1081 *Geology*, 14(8/9), 1059–1077. [https://doi.org/10.1016/0191-8141\(92\)90036-V](https://doi.org/10.1016/0191-8141(92)90036-V)
- 1082 Poirier, J.-P. (1975). On the Slip Systems of Olivine. *Journal of Geophysical Research*, 80(29), 4059–4061.
- 1083 Poirier, J.-P. (1982). On transformation plasticity. *Journal of Geophysical Research*, 87(B8), 6791–6797.
- 1084 Poirier, J.-P. (1985). *Creep of crystals: High-temperature deformation processes in Metals, ceramics and minerals*.
 1085 Cambridge University Press.
- 1086 Poirier, J.-P. (1995). Mineral physics and. In T. J. Ahrens (Ed.), *Mineral physics and crystallography: a handbook*
 1087 *of physical constants* (pp. 245–252). American Geophysical Union. [https://doi.org/10.4324/9780203121146-](https://doi.org/10.4324/9780203121146-35)
 1088 35
- 1089 Poirier, J.-P., & Nicolas, A. (1975). Deformation-Induced Recrystallization Due to Progressive Misorientation of
 1090 Subgrains, with Special Reference to Mantle Peridotites. *The Journal of Geology*, 83(6), 707–720.
 1091 <https://doi.org/10.1086/628163>
- 1092 Précigout, J., & Hirth, G. (2014). B-type olivine fabric induced by grain boundary sliding. *Earth and Planetary*
 1093 *Science Letters*, 395, 231–240. <https://doi.org/10.1016/j.epsl.2014.03.052>
- 1094 Qi, C., Hansen, L. N., Wallis, D., Holtzman, B. K., & Kohlstedt, D. L. (2018). Crystallographic Preferred
 1095 Orientation of Olivine in Sheared Partially Molten Rocks: The Source of the “a-c Switch.” *Geochemistry,*
 1096 *Geophysics, Geosystems*, 19(2), 316–336. <https://doi.org/10.1002/2017GC007309>
- 1097 Raleigh, C. B. (1967). Plastic Deformation of Upper Mantle Silicate Minerals. *Geophysical Journal of the Royal*
 1098 *Astronomical Society*, 14, 45–49. <https://doi.org/10.1111/j.1365-246X.1967.tb06220.x>
- 1099 Raterron, P., Doukhan, N., Jaoul, O., & Doukhan, J. C. (1994). High temperature deformation of diopside IV:
 1100 predominance of {110} glide above 1000°C. *Physics of the Earth and Planetary Interiors*, 82, 209–222.
 1101 [https://doi.org/10.1016/0031-9201\(94\)90073-6](https://doi.org/10.1016/0031-9201(94)90073-6)
- 1102 Raterron, Paul, & Jaoul, O. (1991). High-temperature deformation of diopside single crystal: 1. Mechanical data.
 1103 *Journal of Geophysical Research: Solid Earth*, 96(B9), 14277–14286. <https://doi.org/10.1029/91JB01205>
- 1104 Raterron, Paul, Chen, J., Geenen, T., & Girard, J. (2011). Pressure effect on forsterite dislocation slip systems:
 1105 Implications for upper-mantle LPO and low viscosity zone. *Physics of the Earth and Planetary Interiors*,
 1106 188(1–2), 26–36. <https://doi.org/10.1016/j.pepi.2011.06.009>
- 1107 van Roermund, H. L. M., & Boland, J. N. (1981). The dislocation substructures of naturally deformed omphacites.
 1108 *Tectonophysics*, 78, 403–418.
- 1109 Ruggles, T. J., & Fullwood, D. T. (2013). Estimations of bulk geometrically necessary dislocation density using
 1110 high resolution EBSD. *Ultramicroscopy*, 133, 8–15. <https://doi.org/10.1016/j.ultramic.2013.04.011>
- 1111 Ruzicka, A. M., & Hugo, R. C. (2018). Electron backscatter diffraction (EBSD) study of seven heavily
 1112 metamorphosed chondrites: Deformation systematics and variations in pre-shock temperature and post-shock
 1113 annealing. *Geochimica et Cosmochimica Acta*, 234, 115–147. <https://doi.org/10.1016/j.gca.2018.05.014>
- 1114 Satsukawa, T., & Michibayashi, K. (2009). Determination of slip system in olivine based on crystallographic
 1115 preferred orientation and subgrain-rotation axis: examples from Ichinomegata peridotite xenoliths, Oga
 1116 peninsula, Akita prefecture. *The Journal of the Geological Society of Japan*, 115(6), 288–291.
 1117 <https://doi.org/10.5575/geosoc.115.288>
- 1118 Sciences, P. (1978). The mechanisms of creep in olivine. *Philosophical Transactions of the Royal Society of*
 1119 *London. Series A, Mathematical and Physical Sciences*, 288(1350), 99–119.
 1120 <https://doi.org/10.1098/rsta.1978.0008>
- 1121 Skemer, P., Katayama, I., Jiang, Z., & Karato, S. I. (2005). The misorientation index: Development of a new method
 1122 for calculating the strength of lattice-preferred orientation. *Tectonophysics*, 411(1–4), 157–167.
 1123 <https://doi.org/10.1016/j.tecto.2005.08.023>
- 1124 Skrotzki, W. (1994). Defect structure and deformation mechanisms in naturally deformed augite and enstatite.
 1125 *Tectonophysics*, 229(1–2), 43–68. [https://doi.org/10.1016/0040-1951\(94\)90005-1](https://doi.org/10.1016/0040-1951(94)90005-1)
- 1126 Soustelle, V., & Manthilake, G. (2017). Deformation of olivine-orthopyroxene aggregates at high pressure and
 1127 temperature: Implications for the seismic properties of the asthenosphere. *Tectonophysics*, 694, 385–399.
 1128 <https://doi.org/10.1016/j.tecto.2016.11.020>
- 1129 Stocker, R. L., & Ashby, M. F. (1973). On the rheology of the upper mantle. *Reviews of Geophysics and Space*
 1130 *Physics*, 11(2), 391–426.
- 1131 Stöffler, D., Hamann, C., & Metzler, K. (2018). Shock metamorphism of planetary silicate rocks and sediments:

- 1132 Proposal for an updated classification system. *Meteoritics and Planetary Science*, 53(1), 5–49.
1133 <https://doi.org/10.1111/maps.12912>
- 1134 Sundberg, M., & Cooper, R. F. (2008). Crystallographic preferred orientation produced by diffusional creep of
1135 harzburgite: Effects of chemical interactions among phases during plastic flow. *Journal of Geophysical*
1136 *Research: Solid Earth*, 113(12), 1–16. <https://doi.org/10.1029/2008JB005618>
- 1137 Tasaka, M., Michibayashi, K., & Mainprice, D. (2008). B-type olivine fabrics developed in the fore-arc side of the
1138 mantle wedge along a subducting slab. *Earth and Planetary Science Letters*, 272(3–4), 747–757.
1139 <https://doi.org/10.1016/j.epsl.2008.06.014>
- 1140 Tedonkenfack, S. S. T., Puziewicz, J., Aulbach, S., Ntaflos, T., Kaczmarek, M. A., Matusiak-Malek, M., et al.
1141 (2021). Lithospheric mantle refertilization by DMM-derived melts beneath the Cameroon Volcanic Line—a
1142 case study of the Befang xenolith suite (Oku Volcanic Group, Cameroon). *Contributions to Mineralogy and*
1143 *Petrology*, 176(5), 1–18. <https://doi.org/10.1007/s00410-021-01796-3>
- 1144 Treiman, A. H. (2005). The nakhlite meteorites: Augite-rich igneous rocks from Mars. *Chemie Der Erde -*
1145 *Geochemistry*, 65(3), 203–270. <https://doi.org/10.1016/j.chemer.2005.01.004>
- 1146 Udry, A., & Day, J. M. D. (2018). 1.34 billion-year-old magmatism on Mars evaluated from the co-genetic nakhlite
1147 and chassignite meteorites. *Geochimica et Cosmochimica Acta*, 238, 292–315.
1148 <https://doi.org/10.1016/J.GCA.2018.07.006>
- 1149 Udry, A., Howarth, G. H., Herd, C., Day, J. M. D., Lapen, T. J., & Filiberto, J. (2020). What martian meteorites
1150 reveal about the interior and surface of Mars. *Journal of Geophysical Research: Planets*, 125,
1151 e2020JE006523. <https://doi.org/10.1029/2020JE006523>
- 1152 Ulrich, S., & Mainprice, D. (2005). Does cation ordering in omphacite influence development of lattice-preferred
1153 orientation? *Journal of Structural Geology*, 27(3), 419–431. <https://doi.org/10.1016/j.jsg.2004.11.003>
- 1154 Vollmer, F. W. (1990). An application of eigenvalue methods to structural domain analysis. *Bulletin of the*
1155 *Geological Society of America*, 102(6), 786–791. [https://doi.org/10.1130/0016-](https://doi.org/10.1130/0016-7606(1990)102<0786:AAOEMT>2.3.CO;2)
1156 [7606\(1990\)102<0786:AAOEMT>2.3.CO;2](https://doi.org/10.1130/0016-7606(1990)102<0786:AAOEMT>2.3.CO;2)
- 1157 Watt, L. E., Bland, P. A., Prior, D. J., & Russell, S. S. (2006). Fabric analysis of Allende matrix using EBSD.
1158 *Meteoritics and Planetary Science*, 41(7), 989–1001. <https://doi.org/10.1111/j.1945-5100.2006.tb00499.x>
- 1159 Wenk, H.-R., & Tomé, C. N. (1999). Modeling dynamic recrystallization of olivine aggregates deformed in simple
1160 shear. *Journal of Geophysical Research: Solid Earth*, 104(B11), 25513–25527.
1161 <https://doi.org/10.1029/1999jb900261>
- 1162 Van Der Werf, T., Chatzaras, V., Marcel Kriegsman, L., Kronenberg, A., Tikoff, B., & Drury, M. R. (2017).
1163 Constraints on the rheology of the lower crust in a strike-slip plate boundary: Evidence from the San Quintín
1164 xenoliths, Baja California, Mexico. *Solid Earth*, 8(6), 1211–1239. <https://doi.org/10.5194/se-8-1211-2017>
- 1165 Winiarski, B., Gholinia, A., Mingard, K., Gee, M., Thompson, G., & Withers, P. J. (2021). Correction of artefacts
1166 associated with large area EBSD. *Ultramicroscopy*, 226(March), 113315.
1167 <https://doi.org/10.1016/j.ultramic.2021.113315>
- 1168 Woodward, C. (2005). Plasticity at the Atomic Scale: Parametric, Atomistic, and Electronic Structure Methods.
1169 *Handbook of Materials Modeling*, 2865–2869. https://doi.org/10.1007/978-1-4020-3286-8_171
- 1170 Yao, Z., Qin, K., Wang, Q., & Xue, S. (2019). Weak B-Type Olivine Fabric Induced by Fast Compaction of Crystal
1171 Mush in a Crustal Magma Reservoir. *Journal of Geophysical Research: Solid Earth*, 124(4), 3530–3556.
1172 <https://doi.org/10.1029/2018JB016728>
- 1173 Zhang, J., & Green, H. W. (2007). Experimental investigation of eclogite rheology and its fabrics at high
1174 temperature and pressure. *Journal of Metamorphic Geology*, 25, 97–115. [https://doi.org/10.1111/j.1525-](https://doi.org/10.1111/j.1525-1314.2006.00684.x)
1175 [1314.2006.00684.x](https://doi.org/10.1111/j.1525-1314.2006.00684.x)
- 1176 Zhang, J., Green II, H. W., & Bozhilov, K. N. (2006). Rheology of omphacite at high temperature and pressure and
1177 significance of its lattice preferred orientations. *Earth and Planetary Science Letters*, 246, 432–443.
1178 <https://doi.org/10.1016/j.epsl.2006.04.006>
- 1179